Rare Met. (2025) 44(12):9986–10006
https://doi.org/10.1007/s12598-025-03636-w

RARE METALS

ORIGINAL ARTICLE

Scalable one-pot spray pyrolysis with in situ polymerization for uniform yolk–shell microspheres: novel formation mechanism and application as high-performance potassium-ion battery anodes

Tae Ha Kim, Sang-Hyun Kim, Jung Sang Cho*, Yun Chan Kang*, Gi Dae Park*

Received: 9 May 2025 / Revised: 18 August 2025 / Accepted: 21 August 2025 / Published online: 6 November 2025

Abstract Yolk–shell structures, defined by their core@void@shell architecture, have garnered considerable interest due to their tunable physical and chemical properties, which make them suitable for applications in nanoreactors, drug delivery, energy storage, biosensing, and surface-enhanced Raman scattering. However, conventional synthesis techniques, such as templating and non-templating liquid-phase methods, are often labor-intensive, time-consuming, and challenging to scale. Recently, spray pyrolysis has gained attention as a rapid, one-pot, and continuous synthesis method offering high scalability and production efficiency. This study presents a novel strategy for synthesizing uniform yolk–shell microspheres via spray pyrolysis, augmented by in situ polymerization and the addition of a drying control agent. By systematically varying carbon sources, including citric acid, ethylene glycol, sucrose, and polyvinylpyrrolidone, their influence on particle size distribution and yolk–shell formation were investigated. A novel formation mechanism involving metal–metal oxide–carbon intermediates was proposed to explain the observed morphologies. This approach led to enhanced spherical uniformity and structural consistency, supported by the use of drying control agents. As a case study, nickel oxide yolk–shell particles were synthesized and subsequently converted into nickel sulfide@C microspheres, which exhibited promising performances as anode materials in potassium-ion batteries. Overall, this method provides a scalable, efficient, and versatile route for fabricating yolk–shell structures with customizable features for advanced technological applications.

Keywords Yolk–shell structures; Size distribution control; Carbon sources; Spray pyrolysis; Potassium-ion batteries

Tae Ha Kim and Sang-Hyun Kim have contributed equally to this work.

Supplementary Information The online version contains supplementary material available at https://doi.org/10.1007/s12598-025-03636-w.

T. H. Kim, G. D. Park
Department of Urban, Energy, and Environmental Engineering, Chungbuk National University, Chungdae-ro 1, Seowon-Gu, Cheongju, Chungbuk 28644, Republic of Korea

S.-H. Kim, G. D. Park*
Department of Advanced Materials Engineering, Chungbuk National University, Chungdae-ro 1, Seowon-Gu, Cheongju, Chungbuk 28644, Republic of Korea
e-mail: gdpark@chungbuk.ac.kr

J. S. Cho*
Department of Engineering Chemistry, Chungbuk National University, Chungdae-ro 1, Seowon-Gu, Cheongju, Chungbu 28644, Republic of Korea
e-mail: jscho@cbnu.ac.kr

J. S. Cho, G. D. Park
Advanced Energy Research Institute, Chungbuk National University, Chungdae-ro 1, Seowon-Gu, Cheongju, Chungbuk 28644, Republic of Korea

Y. C. Kang*
Department of Materials Science and Engineering, Korea University, Anam-Dong, Seongbuk-Gu, Seoul 136-713, Republic of Korea
e-mail: yckang@korea.ac.kr

1 Introduction

Yolk–shell, or so-called "ball-in-ball," structures have attracted significant attention as a unique class of core/shell structures characterized by a core@void@shell

configuration. These structures have captivated scientists and engineers not only due to their intriguing structures but also because of their tunable physical and chemical properties [1–3]. Their customizable cores and hollow shells enable the development of new functionalities, making them highly attractive for a wide range of applications, including nanoreactors [4–6], drug/gene delivery [7–9], rechargeable batteries [10–12], biosensors [13–15], surface-enhanced Raman scattering [16–18], and as fundamental building blocks for supra-nanostructures.

Various synthesis strategies have been developed to fabricate yolk–shell structures, including both templating and non-templating methods in liquid phases, as well as gas-phase approaches like the carbon combustion method [19–21]. Among these, selective etching, a representative liquid-phase method, enables precise control over configuration, size, and composition. However, it faces inherent limitations such as the use of highly toxic acids, cumbersome multi-step processes, and difficulties in scaling up [22, 23]. To overcome these challenges, alternative non-templating approaches [24] have been explored, such as self-assembly [25], Ostwald ripening [26], galvanic replacement [27], and Kirkendall diffusion methods [28]. These methods offer facile and versatile pathways for fabricating yolk–shell structures with tunable inner voids and shell morphologies. However, liquid-phase techniques generally involve lengthy reaction times and require additional separation and thermal post-treatment steps [29, 30].

To address the challenges of slow reaction kinetics and low production efficiency, a novel fabrication approach utilizing spray pyrolysis has been developed. This technique enables the rapid and scalable synthesis of yolk–shell structures through a continuous, one-pot process. Kang et al. were the first to report the facile synthesis of metal oxide yolk–shell powders using spray pyrolysis [31]. Subsequently, Wang et al. introduced porous Co_3O_4 yolk–shell microspheres via spray pyrolysis, employing a carbon combustion mechanism [32]. John et al. also demonstrated the formation of hollow and yolk–shell α-Fe_2O_3 microspheres using sucrose as the carbon source [33]. In this method, droplets containing metal ions and sucrose, generated by an ultrasonic nebulizer, were transported into a high-temperature furnace, where they decomposed into metal oxide–carbon composites as intermediates. Under an oxygen-rich atmosphere, the combustion of carbon facilitated the formation of yolk–shell structures. This approach significantly enhances productivity and ensures continuous processing, making it well suited for large-scale manufacturing, as the transformation occurs within seconds. Since these foundational studies, sucrose-based spray pyrolysis has become a predominant route for synthesizing yolk–shell structured metal oxide microspheres [32, 34, 35]. However, because these processes are highly dependent on the droplet size distribution generated by the atomizer, the resulting yolk–shell microspheres inherently reflect the size variability of the metal oxide–carbon composite particles. This leads to a lack of uniformity in the final particle size distribution. While droplet pre-classification has been proposed as a solution, it inevitably reduces overall yield.

To address this limitation, we propose a novel strategy that overcomes the drawbacks of conventional spray pyrolysis methods, which are typically based on the carbon combustion mechanism. Our approach employs a one-pot spray pyrolysis process enhanced by in situ polymerization and the incorporation of a drying control chemical agent (DCCA) to produce yolk–shell microspheres with uniform size distribution. To the best of our knowledge, this is the first study to control yolk–shell size distribution by systematically varying the carbon source. Various carbon sources, including citric acid, ethylene glycol, sucrose, polyvinylpyrrolidone, and their combinations, were introduced into the spray solution, and the resulting particles were comprehensively analyzed.

This work proposes a new formation mechanism for yolk–shell microspheres in spray pyrolysis, involving the generation of intermediate metal–metal oxide–carbon composites. The use of a DCCA was shown to significantly improve the spherical morphology and enhance uniformity in size distribution. This method enables the scalable fabrication of yolk–shell microspheres with narrow size dispersion without sacrificing production yield. As a proof of concept, nickel oxide was selected as the initial target material. After post-treatment, enhanced yolk–shell structured nickel sulfide@C microspheres were successfully synthesized and evaluated as anode materials for potassium-ion batteries to address challenges such as limited capacity, poor stability, and sluggish rate performance [36–40].

2 Experimental

Nanostructured NiO microspheres were synthesized via a one-step spray pyrolysis process. Depending on the combination of additives in the spray solution, the resulting samples were labeled as NiO-Suc, NiO-PVP, NiO-CA, NiO-CA/EG, and NiO-CA/EG/DMF. The spray solution was prepared by dissolving 0.3 M nickel nitrate hexahydrate ($Ni(NO_3)_2{\cdot}6H_2O$) with various additives: 0.1 M citric acid (CA), 0.1 M ethylene glycol (EG), 0.7 M sucrose, 30 g L^{-1} polyvinylpyrrolidone (PVP), and 0.7 M N,N-dimethylformamide (DMF). During the spray pyrolysis process, a 1.7-MHz ultrasonic nebulizer equipped with six vibrators generated fine droplets, which were transported into a preheated quartz reactor (length: 1200 mm; diameter: 50 mm) using air as the carrier gas at a flow rate of 10 L min^{-1}.

To investigate the mechanism of yolk–shell microsphere formation, the spray pyrolysis was conducted at temperatures ranging from 400 to 900 °C. Additional samples, FeO_x-CA/EG/DMF, SnO_x-CA/EG/DMF, and $NiFeO_x$-CA/EG/DMF, were also synthesized using 0.3 M iron nitrate nonahydrate ($Fe(NO_3)_3{\cdot}9H_2O$), 0.3 M Sn(II) oxalate, and a total of 0.3 M Ni and Fe metal salts in a 1:1 molar ratio, while maintaining the same concentrations of CA, EG, and DMF. These were processed following the same spray pyrolysis method used for NiO-CA/EG/DMF.

NiS nanostructures (NiS-CA-800, NiS-Suc-800, NiS-CA/EG/DMF-800, and NiS@C-CA/EG/DMF-800) were synthesized through post-treatment using thiourea as the sulfur source under a 10% H_2/Ar atmosphere at 350 °C for 6 h. To form a carbon surface layer, NiS-CA/EG/DMF-800 was infiltrated with a pitch solution dissolved in tetrahydrofuran (THF) and subjected to an additional heat treatment at 500 °C for 3 h in an Ar atmosphere.

3 Results and discussion

The newly developed formation strategies for uniformly sized yolk–shell microspheres, based on varying carbon sources in the spray pyrolysis process, are systematically illustrated in Scheme 1. The mechanism underlying the formation of yolk–shell structured metal oxide microspheres via the one-pot spray pyrolysis method has been previously reported in detail, as shown in Scheme 1A [31]. In this approach, excess sucrose is introduced into the spray solution relative to the concentration of the metal salt, serving as the primary carbon source. Upon entering the high-temperature reaction furnace, the droplet undergoes rapid decomposition, forming a dense metal oxide–carbon composite. As the process continues, surface carbon combusts, resulting in the formation of an initial metal oxide shell and an interior void. Further passage through the high-temperature zone promotes nanocrystal growth within the shell, oxygen diffusion into the particle, and eventual formation of yolk–shell structures via Ostwald ripening of the inner core.

When citric acid (CA) is employed as the carbon source, the resulting particles are spherical, hollow, and possess thin shells. Acting as a chelating agent, CA modifies the drying and decomposition behavior of the metal salts [41]. The abrupt gas evolution during the decomposition of metal–CA chelates produces hollow precursor particles with relatively large sizes, as illustrated in Scheme 1B. In

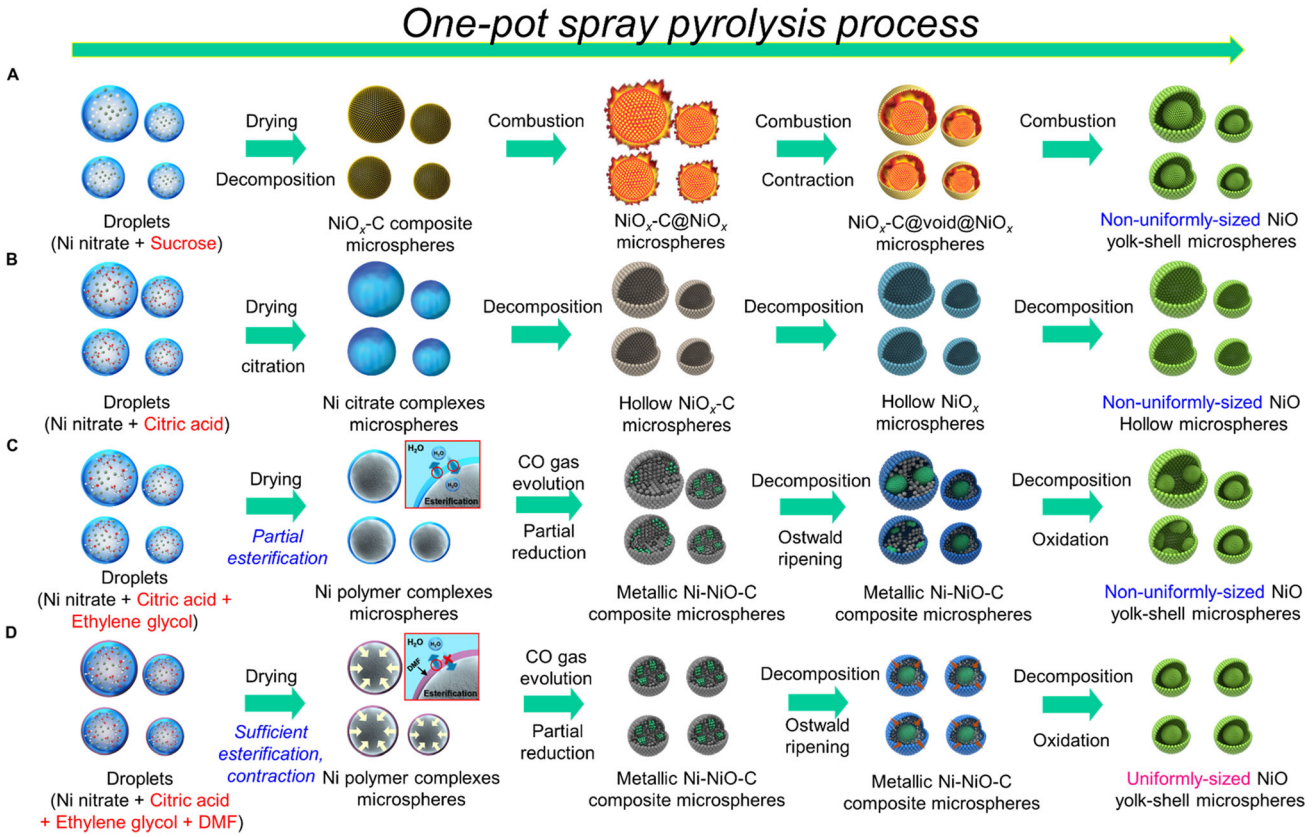

Scheme 1 Schematic illustration of the formation mechanism via the one-pot spray pyrolysis process using a Ni nitrate solution with various carbon sources: **A** sucrose, **B** CA, **C** CA/EG, and **D** CA/EG /DMF

contrast, when CA is combined with EG, an esterification reaction occurs between the carboxyl group of CA and the hydroxyl group of EG within the droplet, generating organic polymers during the initial drying stage [42]. However, the short residence time of the droplets in the reactor hinders complete esterification and prevents sufficient particle densification via reversible esterification in the aqueous phase. This limitation may lead to irregular yolk–shell formation, as shown in Scheme 1C.

Interestingly, this system allows for the proposal of a novel yolk–shell formation mechanism distinct from the traditional carbon combustion route involving sucrose. As the polymer formed by esterification between CA and EG decomposes, it releases a significant amount of CO gas, which acts as a reducing agent. This gas instantaneously reduces NiO nanocrystals to metallic Ni. Driven by Ostwald ripening, the metallic Ni migrates toward the center of the particle during its passage through the high-temperature zone. In the final stage of spray pyrolysis, metallic Ni is re-oxidized, leading to the formation of yolk–shell structured nickel oxide.

To improve morphology and size uniformity, the addition of DMF as a drying control chemical agent significantly enhances the esterification reaction in the aqueous phase [43]. This modification facilitates the densification and size uniformity of the metal–metal oxide–carbon composite intermediate during spray pyrolysis. Ultimately, a highly uniform yolk–shell microsphere is successfully synthesized through this one-pot process, as depicted in Scheme 1D.

To verify the morphologies and size distributions of nickel oxide microspheres synthesized using different carbon sources in the spray pyrolysis process, scanning electron microscope (SEM) images, transmission electron microscope (TEM) images, and dynamic light scattering (DLS) data are presented in Fig. 1. The low-magnification SEM images corresponding to various carbon sources—sucrose, PVP, CA, EG, CA/EG, and CA/EG/DMF—clearly demonstrate the influence of these additives on the shape and distribution of the resulting microspheres. Furthermore, TEM images of NiO microspheres further illustrate their distinct morphological trends depending on the carbon source used. Since spray pyrolysis was conducted in an aqueous solution, the use of carbon sources with high water solubility is necessary to ensure homogeneous precursor dispersion and stable droplet formation. Accordingly, all selected carbon sources were highly water-soluble. Sucrose was employed as a conventional carbon source based on the classical carbon combustion mechanism, serving as a benchmark for comparing particle size distributions. PVP was chosen for its high water solubility and low molecular weight, which make it widely applicable in spray pyrolysis systems.

To evaluate the individual and combined effects of CA, EG, and DMF, additional spray pyrolysis experiments were performed using these additives alone and in combination. Nickel oxide microspheres were synthesized at 800 °C using various carbon sources and were designated as NiO-Suc-800, NiO-PVP-800, NiO-CA-800, NiO-EG-800, NiO-CA/EG-800, and NiO-CA/EG/DMF-800, respectively. NiO-Suc-800 microspheres, produced using sucrose, exhibited typical yolk–shell morphologies with a broad size distribution, as shown in Fig. 1A–D. The droplets formed from the spray system, which contained excess sucrose, displayed a wide range of sizes. Following drying, decomposition, and carbon combustion, this variation was directly translated into the final particle size distribution of the NiO microspheres.

PVP, a low molecular weight polymer with excellent water solubility, was also investigated. During spray pyrolysis, PVP migrated toward the periphery of the droplet due to phase segregation, while some remained within the core along with nickel oxide nanocrystals. Upon carbonization, the PVP-rich outer layer rapidly contracted, leading to the irregular, squishy morphology of NiO-PVP-800 observed in Fig. 1E–G. However, the phase segregation behavior of PVP prevented the formation of a well-defined yolk–shell structure.

NiO-CA-800 and NiO-EG-800 microspheres, synthesized using CA and EG individually as carbon sources, exhibited hollow inner structures with thin shells, as shown in Fig. 1I–K and M–O. The low molecular weights and rapid decomposition rates of CA and EG limited their integration with the metal precursors, resulting in rapid gas evolution and hollow particle formation. Conversely, when CA and EG were used in combination, esterification reactions during spray pyrolysis facilitated densification of the microspheres during droplet drying and decomposition. However, the limited residence time of the droplets in the reactor hindered complete esterification, preventing the particles from achieving sufficient density via reversible esterification in the aqueous phase. Consequently, conditions were not optimal for forming yolk–shell structures, which require a dense metal–metal oxide–carbon intermediate. As shown in Fig. 1Q–S, several NiO-CA/EG-800 microspheres lacked the characteristic yolk–shell structure, despite exhibiting a more uniform size distribution overall.

Conversely, SEM images of NiO-CA/EG/DMF microspheres (Fig. 1U–W) clearly demonstrate that the addition of an appropriate amount of DMF as a drying control chemical additive significantly enhanced the esterification reaction in aqueous solution. This improvement promoted densification and uniformity of the intermediate metal–metal oxide–carbon composite during spray pyrolysis.

DLS measurements of the average hydrodynamic size (D_{av}) of the synthesized nickel oxide microspheres,

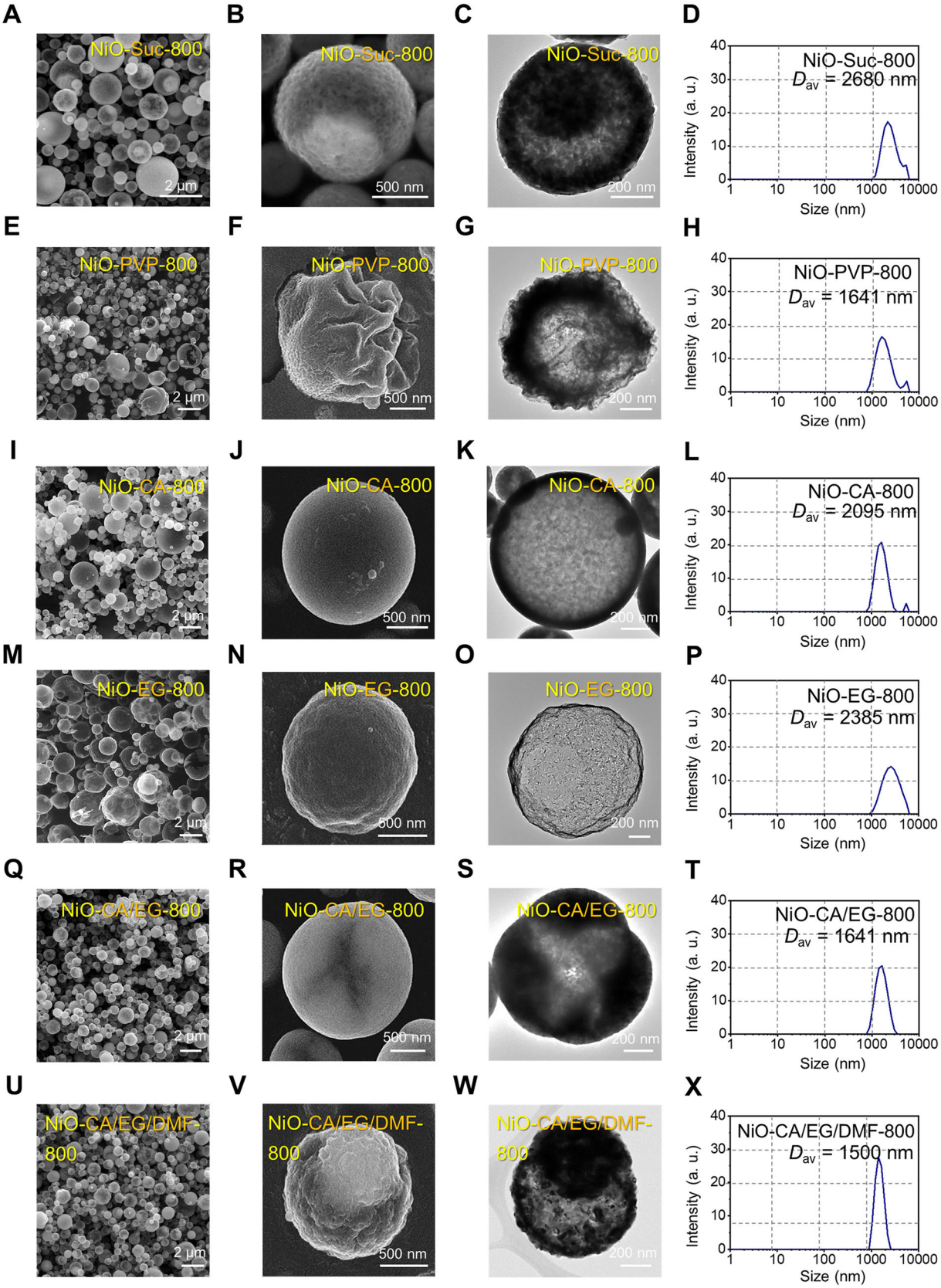

Fig. 1 SEM and TEM images along with DLS data for **A**–**D** NiO-Suc-800, **E**–**H** NiO-PVP-800, **I**–**L** NiO-CA-800, **M**–**P** NiO-EG-800, **Q**–**T** NiO-CA/EG-800, and **U**–**X** NiO-CA/EG/DMF-800

performed in deionized water, further support the conclusion that in situ polymerization and the use of a drying control agent in a one-pot spray pyrolysis process are crucial for forming uniformly sized yolk–shell structures. Detailed statistical data, including D_{av} and polydispersity index (PDI), are summarized in Table S1. Among the samples, NiO-CA/EG/DMF-800 exhibited the narrowest size distribution, with a PDI of approximately 0.039, while NiO-CA/EG-800 also showed relatively uniform particle sizes, with a PDI of approximately 0.073. These findings strongly suggest that in situ polymerization through esterification reactions involving CA, EG, and DMF represents an effective strategy for synthesizing yolk–shell microspheres with highly uniform particle size distributions.

The novel formation mechanism of yolk–shell structured microspheres containing metallic Ni—achieved by simultaneously applying CA, EG, and DMF in the spray solution during the one-pot spray pyrolysis process—was demonstrated through the morphological, crystalline, and magnetic properties of various powders synthesized at different temperatures, as shown in Fig. 2. The spray pyrolysis setup consisted of three main components: a spray generator, a hot furnace, and a powder collector. Droplets were transported into the hot furnace, where thermal decomposition of intermediate particles varied according to the synthesis temperature. To distinguish the synthesized samples by temperature, they were labeled as NiO-CA/EG/DMF-temperature. At a low synthesis temperature of 400 °C, NiO-CA/EG/DMF-400 particles were simply dried and exhibited a dense morphology due to the short residence time of the droplets, as shown in Fig. 2A–C. TEM image in Fig. 2C clearly reveals a solid-filled internal structure, indicating that the polymer had not yet decomposed. The digital image in Fig. 2D further shows that the powder collected at 400 °C was non-magnetic.

As the synthesis temperature increased to 500 °C, a noticeable structural transformation occurred inside the microspheres, as shown in Fig. 2E–G. Compared with NiO-CA/EG/DMF-400, NiO-CA/EG/DMF-500 exhibited signs of internal agglomeration. As the synthesis temperature continued to rise from 500 to 800 °C, the internal structure progressively evolved into a single yolk sphere, as observed in the TEM images (Fig. 2G, K, O, and S). Magnetic testing (Fig. 2H, L, P, and T) revealed that NiO-CA/EG/DMF-500 already contained magnetic materials, even though the process was carried out in air. However, at 900 °C, NiO-CA/EG/DMF-900 microspheres exhibited a relatively porous yolk region and significantly diminished magnetic properties, as confirmed in Fig. 2W, X.

This variation in magnetic behavior is further supported by X-ray diffraction (XRD) results shown in Fig. 2Y. As indicated by the magnetic test (Fig. 2D, Y), NiO-CA/EG/DMF-400 exhibited a pure NiO phase (PDF#47-1049), which is inherently non-magnetic. When the synthesis temperature exceeded 500 °C, metallic Ni (PDF#04-0850) began to appear alongside the NiO phase. NiO-CA/EG/DMF-600 displayed the highest intensity peaks for metallic Ni. However, as the temperature increased beyond 600 °C, the metallic Ni content declined, reaching its lowest point in NiO-CA/EG/DMF-900. Magnetic hysteresis (M–H) curves measured via vibrating sample magnetometry (VSM), as shown in Fig. 2Z, further corroborated these findings. NiO-CA/EG/DMF-400 exhibited weak magnetic properties, consistent with Fig. 2D, Y. As the temperature increased to 500 °C, both saturation magnetization (M_s) and remanence (M_r) increased, peaking at NiO-CA/EG/DMF-600, as summarized in Table S2. Specifically, NiO-CA/EG/DMF-600 exhibited the following magnetic parameters: saturation magnetization (M_s) of 8.27 emu g^{-1}, remanence (M_r) of 1.79 emu g^{-1}, and coercivity (H_c) of 178.70 Oe. However, as the synthesis temperature increased from 700 to 900 °C, a gradual reduction in magnetic properties was observed, aligning with XRD data.

This behavior can be attributed to the evolution of CO gas generated by the decomposition of polymers formed through the esterification reaction between CA and EG. The CO gas acted as a reducing agent, facilitating the conversion of NiO to metallic Ni. However, due to the air environment serving as the carrier gas, metallic Ni was gradually re-oxidized to NiO as the temperature rose. As seen in Fig. 2W, the formation of the internal porous yolk structure is attributed to nanoscale Kirkendall diffusion.

To further investigate the yolk–shell formation mechanism, additional samples were synthesized at intermediate temperatures of 550, 650, and 750 °C. As shown in Fig. S1A, B, NiO-CA/EG/DMF-550 displayed more pronounced inner-shell aggregation compared to NiO-CA/EG/DMF-500. XRD data for this sample revealed sharper metallic Ni peaks, indicating enhanced CO gas evolution and progressive NiO reduction within the 500–600 °C range. At 650 °C, NiO-CA/EG/DMF-650 exhibited further internal aggregation and the development of yolk-like structures, accompanied by the most intense metallic Ni peaks among the intermediate samples (Fig. S1C, D, and G). This suggests that Ostwald ripening plays a critical role in particle aggregation and yolk formation within the 600–700 °C range. Finally, as shown in Fig. S1E, F, NiO-CA/EG/DMF-750 displayed morphology similar to NiO-CA/EG/DMF-800, but with a notable reduction in metallic Ni peak intensity. This indicates that re-oxidation becomes dominant in the 700–800 °C range, leading to extensive aggregation and the formation of uniform yolk–shell microspheres.

Rietveld refinement analysis provides detailed information on the crystal structure and enables quantification of the phase fractions of Ni and NiO. The refinement

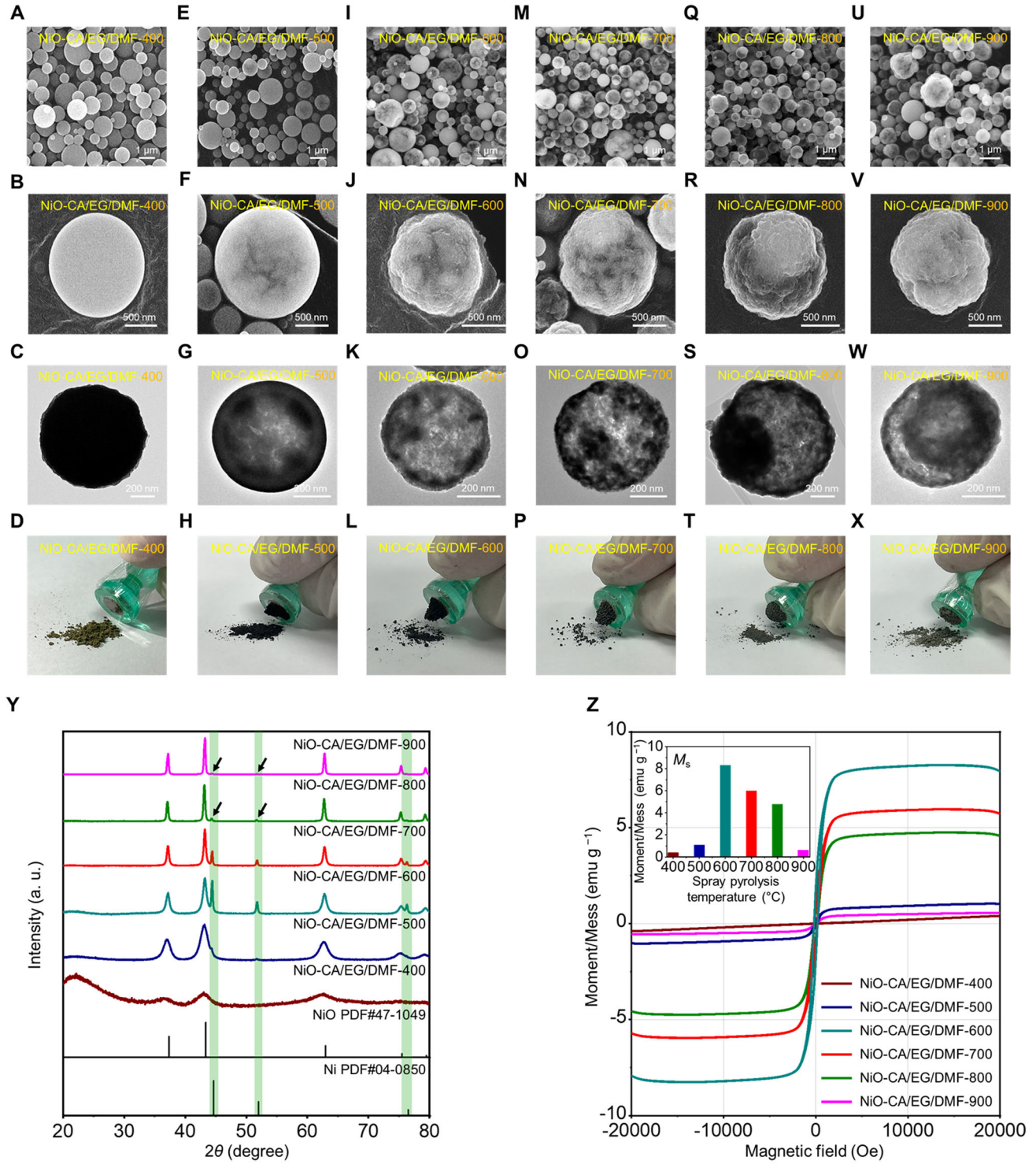

Fig. 2 SEM and TEM images of **A**–**C** NiO-CA/EG/DMF-400, **E**–**G** NiO-CA/EG/DMF-500, **I**–**K** NiO-CA/EG/DMF-600, **M**–**O** NiO-CA/EG/DMF-700, **Q**–**S** NiO-CA/EG/DMF-800, and **U**–**W** NiO-CA/EG/DMF-900. **D**, **H**, **L**, **P**, **T**, **X** Magnetic test images of NiO-CA/EG/DMF synthesized at different spray pyrolysis temperatures. **Y** XRD patterns and **Z** VSM data of NiO-CA/EG/DMF synthesized at different spray pyrolysis temperatures

results for NiO-CA/EG/DMF samples synthesized at various spray pyrolysis temperatures, ranging from 400 to 900 °C, are shown in Fig. S2. According to the NiO PDF card, all samples crystallized in a face-centered cubic crystal structure with space group $Fm\bar{3}m$ (space group number 225) and a lattice parameter of $a = 4.180$ Å.

Metallic Ni also adopts a face-centered cubic structure with the same space group, $Fm\bar{3}m$ (space group number 225), and a lattice parameter of $a = 3.52510$ Å. The detailed refinement results, including phase fractions, lattice parameters, cell volumes, and other refined parameters, are summarized in Table S3. NiO-CA/EG/DMF-400 exhibited only broad NiO peaks in XRD pattern, indicating an early-stage structure with limited crystallinity. As the temperature increased to 500 °C, weak metallic Ni peaks emerged, corresponding to a minor phase fraction of 2.35%. At 600 °C, coinciding with the onset of yolk–shell formation, the metallic Ni fraction significantly increased to 20.37%, as confirmed by Rietveld refinement. This trend is consistent with the XRD and VSM results, where the metallic Ni content increased up to 600 °C and subsequently declined with further temperature elevation. Specifically, the Ni phase fractions were 12.43%, 3.90%, and 0.84% at 700, 800, and 900 °C, respectively. Interestingly, the lattice parameter of NiO increased in parallel with the rising metallic Ni content, likely due to tensile lattice strain at the Ni/NiO interface caused by partial reduction and structural interaction [44].

To optimize additional key parameters influencing the formation of uniform yolk–shell microspheres, including precursor concentration and residence time, different concentrations of precursors were synthesized. At a low precursor concentration (0.1 M, denoted as 0.1 M-NiO-CA/EG/DMF-800), yolk–shell structures were absent, as shown in Fig. S3A, B. Although weak metallic Ni peaks appeared in XRD patterns, SEM images revealed that insufficient Ni content hindered inner-shell agglomeration. Conversely, at a high concentration (0.5 M, denoted as 0.5 M-NiO-CA/EG/DMF-800), excessive Ni content inhibited effective reduction and contraction. As shown in Fig. S3C, D, SEM images display dense, compact microspheres, while the XRD patterns exhibit only NiO peaks, indicating suppression of CO gas-induced NiO reduction, as seen in Fig. S3E. Furthermore, in the case of carrier gas flow rate, which directly affects residence time, at a slower rate of 5 L min^{-1} (denoted as 5 L-NiO-CA/EG/DMF-800), yolk–shell morphologies were maintained, but longer residence times increased crystallinity and promoted re-oxidation, as indicated by diminished metallic Ni peaks in XRD in Fig. S4A, B, and E. In contrast, a faster flow rate of 20 L min^{-1} (denoted as 20 L-NiO-CA/EG/DMF-800) shortened residence time, resulting in incomplete reactions, as shown in Fig. S4C, D. The resulting sample contained a mixture of well-formed yolk–shells, partially agglomerated particles, and dense spheres. Notably, its XRD pattern showed strong metallic Ni peaks, similar to that of NiO-CA/EG/DMF-600, suggesting insufficient re-oxidation under fast flow conditions, as shown in Fig. S4E. These results collectively confirm that precise control of temperature, precursor concentration, and carrier gas flow rate is essential to achieving uniform yolk–shell microsphere formation during spray pyrolysis. To demonstrate the effect of metallic Ni formation based on different carbon sources during the spray pyrolysis process, the morphologies, crystal structures, and magnetic properties of samples synthesized using sucrose, CA, EG, and CA/EG as carbon sources were evaluated, as shown in Fig. S5. The samples were produced at a synthesis temperature of 600 °C, where the highest magnetic properties were observed when CA/EG/DMF was used as the carbon source. These samples were designated as NiO-Suc-600, NiO-CA-600, NiO-EG-600, and NiO-CA/EG-600, respectively. As shown in Fig. S5A, B, the SEM images of NiO-Suc-600 revealed a solid-filled structure, whereas NiO-CA-600 and NiO-EG-600 exhibited hollow-structured microspheres, as shown in Fig. S5D, E, G, and H. The magnetic test results, presented in Fig. S5C, F, and I, confirmed that these samples were non-magnetic, which was further supported by XRD and *M-H* curves in Fig. S5M, N. However, NiO-CA/EG-600 exhibited a slightly agglomerated core region, and the magnetic test results, as shown in Fig. S5J-L, along with XRD and M-H curves, indicated the presence of metallic Ni, confirming its magnetic properties. Notably, NiO-CA/EG/DMF-600 demonstrated significantly higher M_s and M_r values compared to NiO-CA/EG-600, as confirmed in Table S2. This enhancement can be attributed to the sufficient addition of DMF solvent as a drying control chemical additive, which accelerated the esterification reaction in aqueous solution. This process facilitated the formation of excess CO gas, creating a reducing atmosphere during the spray pyrolysis process, thereby promoting the formation of metallic Ni.

In this novel synthesis mechanism, the evolution of CO gas and the reduction of NiO play crucial roles. To indirectly investigate gas evolution during spray pyrolysis, thermogravimetric analysis coupled with mass spectrometry (TG-MS) was employed to gain insights into gas evolution behavior and thermal decomposition dynamics [45–47]. TG-MS was conducted on NiO-CA/EG/DMF-400 sample, where thermal decomposition is minimal. As shown in Fig. S6, TG-MS data revealed an initial weight loss of approximately 6%, corresponding to the evaporation of residual moisture and by-products from esterification reactions. A significant weight loss ($\sim$ 40.26%) was observed between 300 and 400 °C, after which the weight stabilized, indicating the completion of decomposition and redox processes. This notable weight reduction is attributed to the decomposition of the polymer matrix, the evolution of CO gas, and the simultaneous reduction involving Ni and NiO complexes. Previous studies have reported the formation of intermediate species containing ester bonds and carbonyl groups derived from carboxylic acids and

partially unreacted carboxylic acid functionalities [48–50]. Upon thermal decomposition, these groups release CO, as well as CO_2 and N_xO_y gases. Our TG-MS results align with these findings, further supporting that CO gas evolution during thermal decomposition acts as a reducing agent for NiO. These results indicate that during the thermal decomposition of the NiO–polymer complex, a substantial amount of CO gas is generated, which effectively reduces NiO to metallic Ni.

To explore not only the composition of nickel oxide but also the feasibility of the proposed yolk–shell synthesis mechanism across different compositions, iron, tin, and binary nickel–iron salts were applied to CA, EG, and DMF-based spray solutions and synthesized at 800 °C via the spray pyrolysis process. The resulting samples were designated as FeO_x-CA/EG/DMF-800, SnO_x-CA/EG/DMF-800, and $NiFeO_x$-CA/EG/DMF-800, respectively. The morphologies and crystal structures of FeO_x-CA/EG/DMF-800, SnO_x-CA/EG/DMF-800, and $NiFeO_x$-CA/EG/DMF-800 are presented in Fig. 3. All three samples exhibited yolk–shell structures, and their crystal structures corresponded to Fe_2O_3, SnO_2, and $NiO/NiFe_2O_4$, respectively. To confirm whether the same formation mechanism observed in NiO-CA/EG/DMF could be applied, SnO_x-CA/EG/DMF and FeO_x-CA/EG/DMF powders were also synthesized at 600 and 700 °C via spray pyrolysis, as shown in Fig. S7.

In Fig. S7A, B, SnO_x-CA/EG/DMF-600 exhibited a dense-structured microsphere with a SnO_2 phase, whereas SnO_x-CA/EG/DMF-700 displayed a core–shell structured microsphere consisting of SnO_2 and partially reduced Sn, as shown in Fig. S7E, F, and I. This indicates that metallic Sn was formed by the reduction of SnO_2 at the relatively high temperature of 700 °C, while at 600 °C, metallic Sn was not detected, making the formation of a yolk–shell structure difficult. At 800 °C, yolk–shell structured SnO_x-CA/EG/DMF-800 was rapidly formed through the intermediate metallic Sn phase, which was subsequently oxidized back to SnO_2, as confirmed by XRD data. Similarly, Fig. S7C, D, G, H, and I shows that FeO_x-CA/EG/DMF-600 and FeO_x-CA/EG/DMF-700 displayed partially aggregated core regions due to agglomeration of metallic Fe under the reducing atmosphere. As with SnO_x-CA/EG/DMF, the metallic Fe component was readily oxidized to iron oxide, as verified by XRD results.

The formation of metallic phases resulting from the CO-rich reducing environment, generated by the decomposition of polymers formed through esterification of CA and EG, played a critical role in core agglomeration within the yolk region, ultimately leading to yolk–shell structure formation. In this study, DMF was employed to facilitate sufficient esterification reactions with CA and EG. To further investigate the effects of DMF with other additives, additional spray pyrolysis was conducted at 800 °C by combining DMF with various carbon sources, including sucrose, PVP, CA, and EG, resulting in samples designated as NiO-Suc/DMF-800, NiO-PVP/DMF-800, NiO-CA/DMF-800, and NiO-EG/DMF-800, respectively.

However, in the cases of sucrose, PVP, and EG, no significant polymerization reactions with DMF were observed. Consequently, the morphologies of these samples closely resembled those of their counterparts synthesized without DMF, as shown in Fig. S8A–H. This observation is further supported by XRD analysis, where NiO-Suc/DMF-800, NiO-PVP/DMF-800, and NiO-EG/DMF-800 exhibit only NiO phases, indicating the absence of DMF-induced chemical transformation, as shown in Fig. S8I. Notably, NiO-PVP/DMF-800 displayed more pronounced shrunken shell morphologies compared to NiO-PVP-800. This can be attributed to the stabilizing effect of DMF on PVP in solution, which likely promotes its outward migration during droplet evaporation and thermal decomposition [51, 52].

Notably, NiO-CA/DMF-800 exhibits significantly different morphologies compared to NiO-CA-800. As shown in Fig. S8E, F, SEM images of NiO-CA/DMF-800 display yolk–shell-like structures similar to those observed in NiO-CA/EG/DMF-800. Although CA does not chemically react with DMF, the presence of DMF in the precursor solution appears to suppress citration during CA decomposition. This effect likely reduces excessive gas evolution, enabling partially undecomposed CA to become entrapped within the microspheres. Subsequent thermal decomposition of the residual CA and the concurrent oxidation of metallic Ni facilitate the formation of yolk–shell-like structures. Furthermore, the XRD pattern of NiO-CA/DMF-800 reveals the presence of metallic Ni peaks, indicating partial reduction by CO gas generated during CA decomposition, as shown in Fig. S8I. However, compared with NiO-CA/EG/DMF-800, NiO-CA/DMF-800 sample displays non-uniform morphologies and incomplete yolk–shell structures among the particles. Therefore, esterification reactions between CA and EG, promoted by the presence of DMF, play a pivotal role in generating uniform and fully developed yolk–shell microspheres. The morphological features of the newly proposed yolk–shell structured NiO-CA/EG/DMF-800 microspheres were comprehensively investigated, as illustrated in Fig. 4. Low-magnification TEM images in Fig. 4A, B reveal that the microspheres possess a yolk–shell architecture, while the yolk region exhibits a porous structure, as shown in Fig. 4C. The formation of the porous yolk structure is attributed to the aggregation of metallic Ni nanocrystals, which formed under the reducing atmosphere of CO gas generated during decomposition of the polymers resulting from esterification of CA and EG in the spray pyrolysis process. These

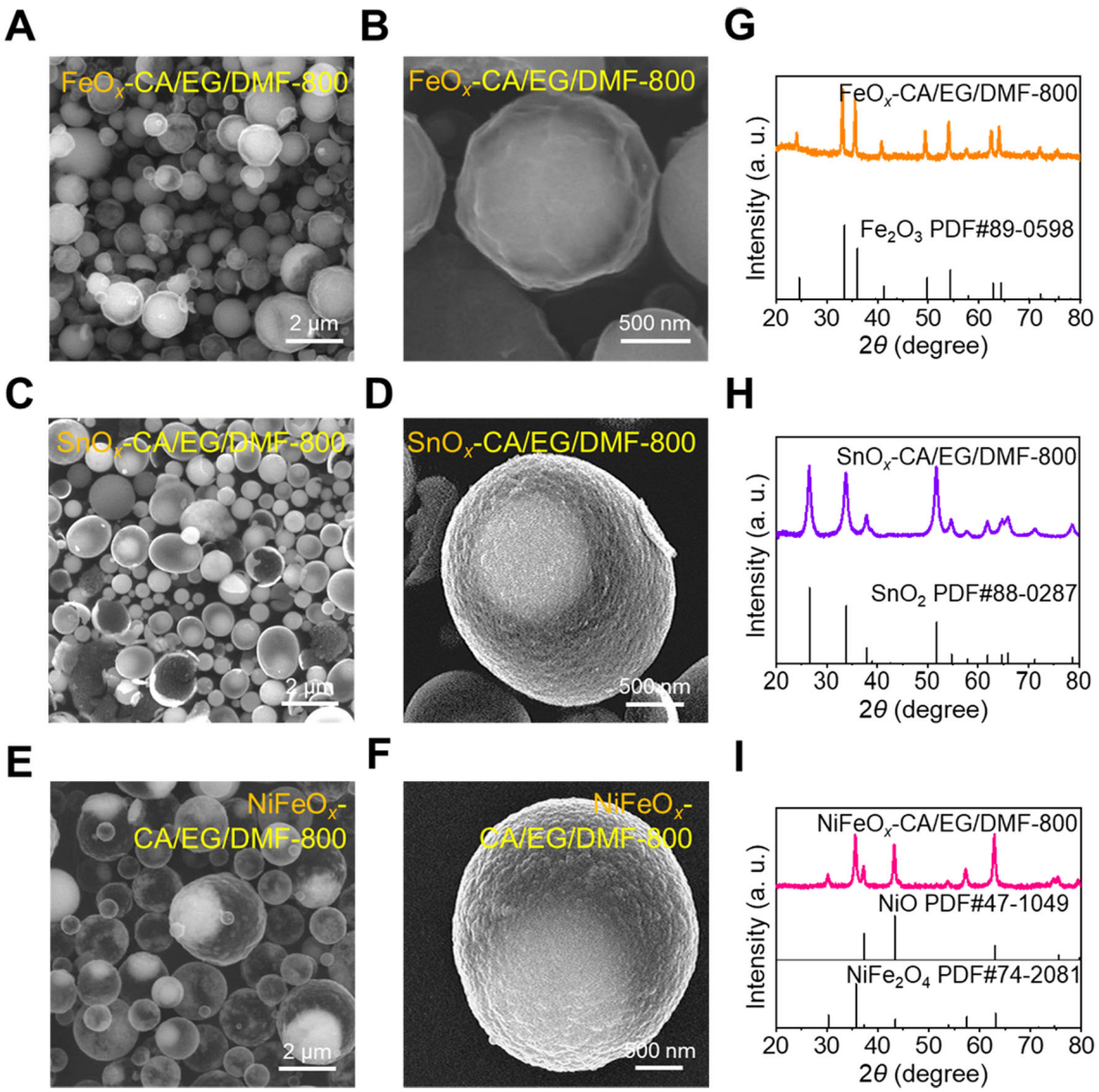

Fig. 3 Morphologies and crystal structures of various metal oxide yolk–shell microspheres: SEM images of **A**, **B** FeO_x-CA/EG/DMF-800, **C**, **D** SnO_x-CA/EG/DMF-800, and **E**, **F** $NiFeO_x$-CA/EG/DMF-800. XRD patterns of **G** FeO_x-CA/EG/DMF-800, **H** SnO_x-CA/EG/DMF-800, and **I** $NiFeO_x$-CA/EG/DMF-800

metallic Ni nanocrystals underwent partial oxidation, giving rise to the porous structure via the well-established nanoscale Kirkendall diffusion mechanism. Furthermore, due to the short residence time caused by the high carrier gas flow rate in the spray pyrolysis process, some aggregated metallic Ni nanocrystals remained in the yolk region without complete oxidation. The high-resolution TEM image in Fig. 4D shows distinct lattice fringes with spacings of 0.24 and 0.20 nm, corresponding to the (111) planes of NiO and metallic Ni, respectively. The selected area electron diffraction (SAED) pattern in Fig. 4E further confirms the coexistence of NiO and metallic Ni phases in NiO-CA/EG/DMF-800. Additionally, elemental mapping images in Fig. 4F demonstrate the successful formation of Ni-NiO yolk–shell structured microspheres. As observed in TEM image in Fig. 4B, a more intense Ni signal in the yolk region suggests a localized concentration of metallic Ni.

To examine additional design parameters influencing yolk and shell size distributions, a quantitative analysis was conducted using multiple TEM images of NiO-CA/EG/DMF-800 and NiO-Suc-800 yolk–shell microspheres. As illustrated in Fig. S9, both samples exhibit a linear correlation between yolk size and overall particle diameter. Notably, NiO-CA/EG/DMF-800 exhibits a larger yolk size, whereas NiO-Suc-800 shows a thicker shell, indicating an inverse relationship between yolk size and shell thickness, as seen in Fig. S9A, B. To further examine structural characteristics, the yolk size-to-shell thickness ratio was

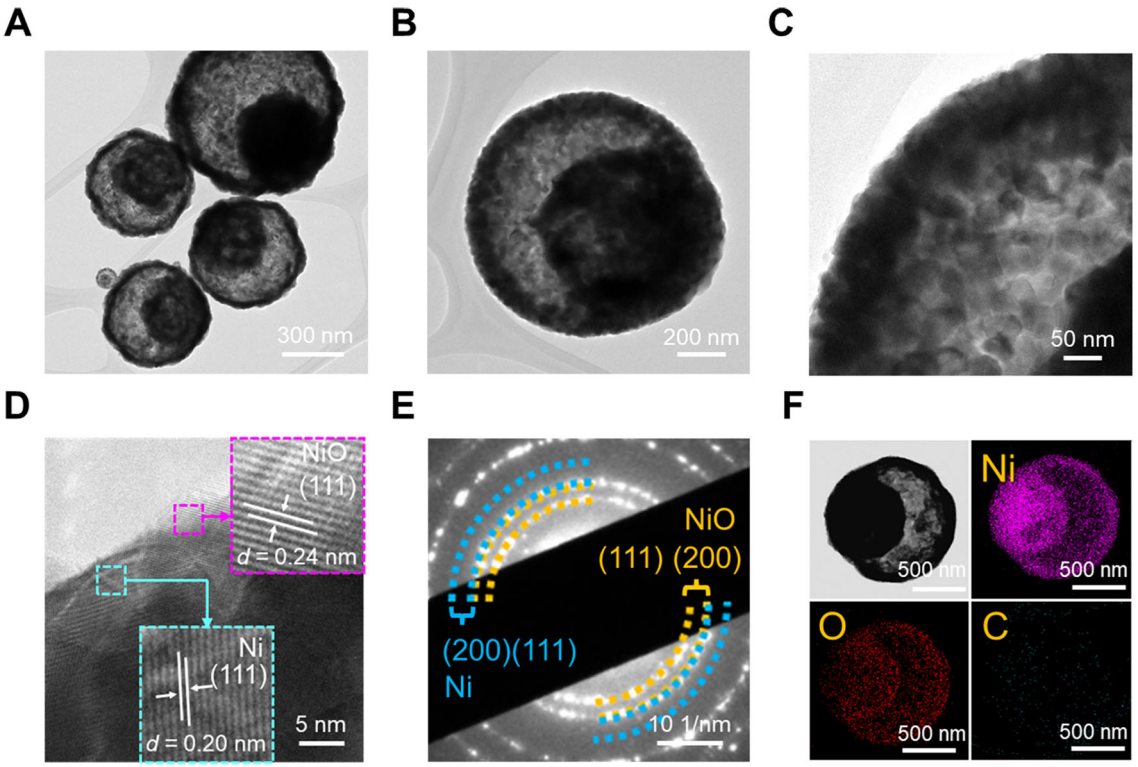

Fig. 4 Detailed characteristics of NiO-CA/EG/DMF-800: **A**–**C** TEM images, **D** HR-TEM image, **E** SAED pattern, and **F** elemental mapping images of NiO-CA/EG/DMF-800

calculated and found to be higher for NiO-CA/EG/DMF-800 than for NiO-Suc-800, as presented in Fig. S9C. This finding clearly confirms that NiO-CA/EG/DMF-800 possesses larger yolks and thinner shells compared to NiO-Suc-800. These structural disparities are attributed to distinct synthesis mechanisms: In NiO-Suc-800, based on carbon combustion, dense shells form due to rapid thermal decomposition and internal carbon combustion; in contrast, the in situ polymerization route of NiO-CA/EG/DMF-800, driven by esterification reactions, promotes homogeneous precursor aggregation throughout the droplet, facilitating the formation of larger yolks and thinner shells. According to prior studies on yolk–shell structures, an optimal shell thickness enhances cycling stability by buffering volumetric changes, while a larger yolk volume contributes to increased energy density [53, 54]. Therefore, the yolk–shell configuration observed in NiO-CA/EG/DMF-800—characterized by a larger yolk and thinner shell—is advantageous for both electrochemical performance and practical applicability in energy storage systems. These uniformly sized yolk–shell microspheres hold promise as anode materials for alkali-ion batteries due to their structural integrity.

Recently, metal sulfide materials have garnered significant interest for potassium-ion batteries due to their high theoretical capacities and more favorable conversion reactions relative to metal oxides [55–57]. However, such materials often suffer from structural degradation and sluggish reaction kinetics [58–60]. To address the inherent limitations of nickel sulfide, including poor stability and limited reaction kinetics, a synergistic strategy was designed involving the integration of uniform NiO yolk–shell structures, sulfidation to nickel sulfide, and post-synthesis carbon coating. This synergistic strategy leverages the high theoretical capacity, higher conductivity, and natural abundance of nickel sulfide, along with the structural uniformity and robustness of the NiO yolk–shell framework, to enhance both the cycling stability and rate performance of potassium-ion battery anodes.

To validate the electrochemical advantages of these uniformly structured yolk–shell microspheres, NiO-CA-800, NiO-Suc-800, and NiO-CA/EG/DMF-800 were subjected to sulfidation under a hydrogen sulfide (H_2S) gas atmosphere, resulting in nickel sulfide–carbon composite microspheres labeled as NiS-CA-800, NiS-Suc-800, and NiS-CA/EG/DMF-800, respectively. The morphological characteristics of these composites are presented in Fig. S10. Following sulfidation, all samples exhibited the crystalline growth of primary nickel sulfide particles on their surfaces. NiS-CA-800 retained a hollow morphology

with a non-uniform size distribution, as shown in Fig. S10A, B. Similarly, NiS-Suc-800 exhibited a yolk–shell structured morphology but also suffered from size irregularities, as illustrated in Fig. S10C, D. Additionally, several larger NiS-CA-800 and NiS-Suc-800 microspheres fractured post-sulfidation. Densely sintered nickel sulfide nanocrystals were also observed within large hollow microspheres with thin shells. In contrast, NiS-CA/EG/DMF-800 demonstrated relatively uniform yolk–shell microspheres with well-dispersed nickel sulfide nanocrystals, as depicted in Fig. S10E, F. This suggests that the uniform yolk–shell precursor structure significantly contributes to the consistent distribution of primary nickel sulfide nanocrystals.

To determine whether the uniformity in size was maintained after sulfidation, DLS analyses were conducted on NiS-CA/EG/DMF-800, NiS-CA-800, and NiS-Suc-800, as shown in Fig. S11. All sulfidized samples displayed broader size distributions compared to their NiO precursors, which is attributed to crystal growth during the sulfidation process. Notably, NiS-CA-800 and NiS-Suc-800 exhibited wider distributions than NiS-CA/EG/DMF-800, reflecting the initial size variability of their respective NiO precursors. Conversely, NiS-CA/EG/DMF-800, derived from a more uniform NiO precursor, retained a relatively narrow particle size distribution post-sulfidation. Interestingly, NiS-CA-800 and NiS-Suc-800 exhibited smaller D_{av} than their NiO counterparts, NiO-CA-800 and NiO-Suc-800, respectively, likely due to non-uniform fracturing during the sulfidation step. The PDI values for all sulfidized samples are summarized in Table S4.

The crystalline structures of NiS-CA-800, NiS-Suc-800, and NiS-CA/EG/DMF-800 were further analyzed by XRD, as shown in Fig. S12. XRD patterns of NiS-CA-800 and NiS-CA/EG/DMF-800 revealed the presence of multiple nickel sulfide phases, including Ni_3S_2, Ni_9S_8, and Ni_7S_6. NiS-Suc-800 sample also exhibited an additional NiS phase. Overall, sulfur-deficient nickel sulfide phases formed during the sulfidation process under H_2S atmosphere at 350 °C.

To gain further insight into the chemical states and molecular environment, X-ray photoelectron spectroscopy (XPS) was performed on NiS-CA/EG/DMF-800, with the results displayed in Fig. S13. In the Ni 2p spectrum (Fig. S13A), primary peaks at 855.3 eV (Ni $2p_{3/2}$) and 873.05 eV (Ni $2p_{1/2}$), along with satellite peaks, are consistent with nickel sulfide phases such as Ni_3S_2, Ni_9S_8, and Ni_7S_6. The observed valence states indicate the presence of nickel ions in Ni_3S_2, Ni_9S_8, and Ni_7S_6 is primarily Ni^{3+}, with some Ni^{2+} species contributing to additional peaks at 852.5 and 869.7 eV for Ni $2p_{3/2}$ and Ni $2p_{1/2}$, respectively [61–63]. In the S 2p spectrum (Fig. S13B), two core-level peaks at 161.3 and 162.5 eV correspond to S $2p_{3/2}$ and S $2p_{1/2}$, respectively, confirming the formation of sulfide species [62, 64].

To enhance the structural stability and electrical conductivity of the uniformly sized NiS-CA/EG/DMF-800 yolk–shell microspheres used as anode materials for potassium-ion batteries, pitch-derived carbon-coated NiS-CA/EG/DMF-800 yolk–shell microspheres (denoted as NiS@C-CA/EG/DMF-800) were synthesized via a simple pitch solution impregnation method, as previously described in the literature. The morphological features of NiS@C-CA/EG/DMF-800 are presented in Figs. S10G, H, and 5. SEM images reveal that the NiS@C-CA/EG/DMF-800 microspheres maintain a morphology similar to that of NiS-CA/EG/DMF-800, as shown in Fig. S10. TEM images in Fig. 5A, B show an increase in the size of the primary nanocrystals forming the yolk–shell microspheres after sulfidation, compared to those shown in Fig. 4A, B. Despite this increase, the yolk–shell structure remains well-preserved post-sulfidation. A thin layer of pitch-derived carbon is visibly coating the microsphere surface, as seen in Fig. 5C. The high-resolution TEM image in Fig. 5D displays clear lattice fringes with spacings of 0.24, 0.18, and 0.28 nm, corresponding to the (062), (044), and (-110) crystal planes of the Ni_7S_6, Ni_9S_8, and Ni_3S_2 phases, respectively. SAED and XRD patterns shown in Figs. 5E and S12 further confirm the coexistence of multiple nickel sulfide phases, including Ni_7S_6, Ni_9S_8, and Ni_3S_2, within the NiS@C-CA/EG/DMF-800 microspheres. Elemental mapping in Fig. 5F verifies the formation of carbon-coated nickel sulfide yolk–shell microspheres.

To validate the superior electrochemical properties of these uniformly sized nickel sulfide yolk–shell microspheres compared to non-uniformly distributed hollow and yolk–shell microspheres, several electrochemical analyses were conducted. First, cyclic voltammetry (CV) was performed on NiS-CA-800, NiS-Suc-800, and NiS-CA/EG/DMF-800 in a potential range of 0.001–3.0 V (versus K^+/K) for the first five cycles at a scan rate of 0.1 mV s^{-1}, as shown in Fig. S14. Although all three nickel sulfide electrodes (NiS-CA-800, NiS-Suc-800, and NiS-CA/EG/DMF-800) contain a mixture of nickel sulfide phases including Ni_7S_6, Ni_9S_8, and Ni_3S_2, their CV curves exhibit nearly identical cathodic and anodic peak positions, as illustrated in Fig. S14A, C, and E. During the initial cathodic sweep, two broad irreversible peaks appear at approximately 0.67 and 0.41 V, attributed to the initial K^+ intercalation, formation of a solid electrolyte interphase (SEI), and the conversion of potassiated nickel sulfide to metallic Ni and potassium sulfide. The disappearance of these peaks in subsequent cycles indicates irreversible capacity loss due to initial potassiation and electrolyte decomposition [65, 66]. The first reduction peak at 0.67 V is associated with the initial insertion of K^+ ions into nickel sulfide

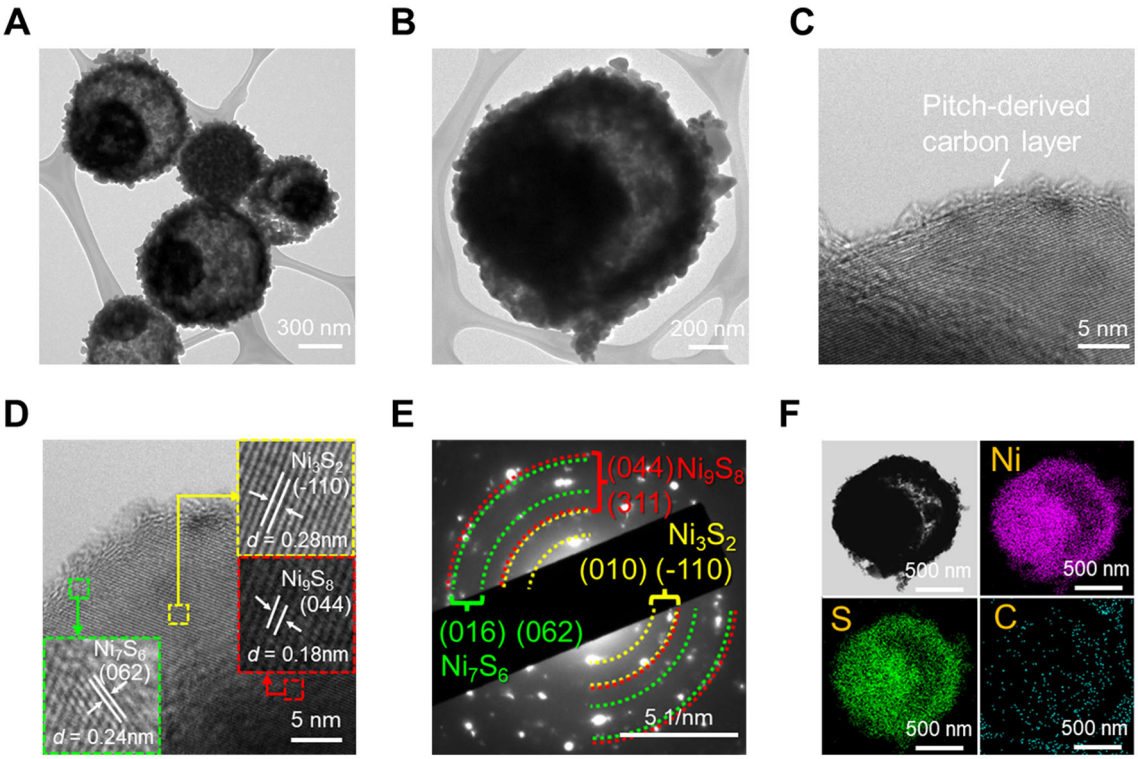

Fig. 5 Detailed characteristics of NiS@C-CA/EG/DMF-800: **A**–**C** TEM images, **D** HR-TEM image, **E** SAED pattern, and **F** elemental mapping images of NiS@C-CA/EG/DMF-800

electrodes and the formation of the intermediate K_xNiS_y phase [67, 68]. Subsequently, through potassium-ion insertion into nickel sulfide, a distinct reduction peak appears at 0.41 V corresponding to the conversion of K_xNiS_y into metallic Ni and potassium sulfide along with SEI formation as a result of electrolyte decomposition [69, 70]. Additionally, minor redox peaks at approximately 0 V appear across all samples, likely due to K^+ insertion/extraction in Super P, the conductive carbon additive used in the electrodes [71]. In the initial anodic sweep, two prominent oxidation peaks at approximately 1.2 and 1.7 V are attributed to the de-potassiation process and the reversible formation of K_xNiS_y and NiS_x phases, respectively [69, 72]. In subsequent cycles, the cathodic peak potentials shift to higher values, which can be ascribed to the transformation of large nickel sulfide crystals into ultrafine nanosized crystals during the initial cycle. From the second to the fifth cycles, the electrodes consistently exhibit reduction peaks near 0.65 V and oxidation peaks at 1.15, 1.55, and 1.76 V, indicating the reversible redox behavior between K^+ and nickel sulfide [73, 74]. The stable positions of these peaks over multiple cycles confirm the electrochemical reversibility and structural stability of the potassium-ion conversion reaction mechanism in these electrodes [73]. The initial galvanostatic discharge/charge curves of the three samples at a current density of 0.2 A g^{-1} align well with the redox peaks observed in the CV profiles, as shown in Fig. S14B, D, and F. The initial discharge capacities for NiS-CA-800, NiS-Suc-800, and NiS-CA/EG/DMF-800 were 799.0, 628.0, and 646.8 mAh g^{-1}, respectively, with corresponding initial Coulombic efficiencies (ICEs) of 71%, 76%, and 80%. These results indicate that the uniformly sized yolk–shell-structured NiS-CA/EG/DMF-800 microspheres facilitate the homogeneous formation of nickel sulfide nanocrystals within the yolk–shell structure, as evidenced in Fig. S10. This structural uniformity enhances the reversibility of active material reactions and improves K^+ diffusion, thereby contributing to a higher ICE value.

The CV curves and initial discharge/charge profiles of NiS@C-CA/EG/DMF-800, presented in Fig. 6A, B, displayed nearly identical cathodic and anodic peaks, along with corresponding plateaus, in comparison with those of NiS-CA/EG/DMF-800 shown in Fig. S14A. This observation confirms that the nickel sulfide phase in NiS@C-CA/EG/DMF-800 was well-maintained following the pitch-derived carbon coating process. The initial discharge and charge capacities were 584.6 mAh g^{-1} and 471.8 mAh g^{-1}, respectively, yielding an initial Coulombic efficiency (ICE) of 81%. These results indicate that the presence of the thin carbon coating layer did not significantly affect the reversibility of the electrochemical reaction between nickel

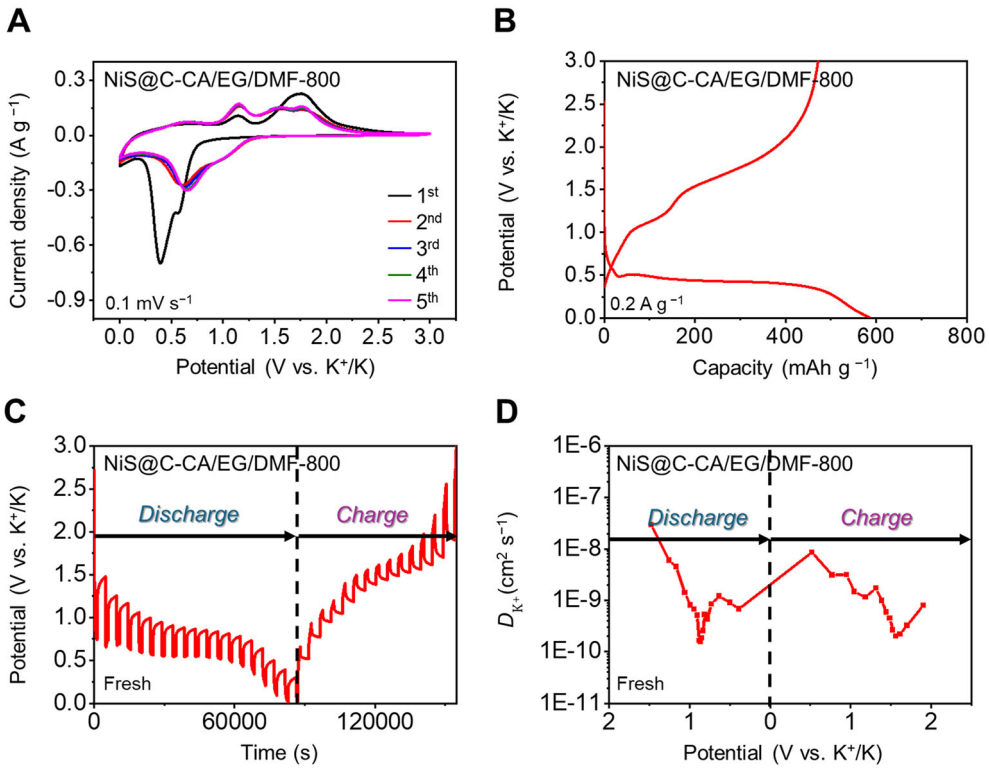

Fig. 6 Electrochemical properties of NiS@C-CA/EG/DMF-800: **A** CV curves, **B** its initial discharge/charge curves, **C** GITT potential profiles, and **D** corresponding potassium-ion diffusion coefficients of NiS@C-CA/EG/DMF-800

sulfide and potassium ions. The potassium-ion diffusion coefficient (D_{K^+}) as a function of potential was further evaluated using the galvanostatic intermittent titration technique (GITT), with the results for NiS@C-CA/EG/DMF-800 illustrated in Fig. 6C, D. During the first cycle, GITT was conducted by applying a constant current density of 0.1 A g^{-1} for 20-min intervals, followed by a 60-min relaxation period, as shown in Fig. 6C. The values of D_{K^+} were calculated using the following equation, based on Fick's second law:

$$D_{K^+} = 4/\pi\tau\left(\frac{m_B V_M}{M_B S}\right)^2 \cdot \left(\frac{\Delta E_s}{\Delta E_\tau}\right)^2 \quad (1)$$

where τ is the duration of the current pulse, m_B and M_B are the molar weight and the mass of the active materials, respectively, V_M is the molar volume, S is the contact area between the electrode and the electrolyte, and E_τ is the potential change during the discharge/charge current pulse, and E_s is the steady-state voltage change after eliminating the IR drop originating from the internal electrical resistance. During the initial potassiation process, the D_{K^+} values demonstrated sharp fluctuations. The initial D_{K^+} values declined until approximately 1.0 V, where potassium ions were intercalated into the nickel sulfide matrix and the pitch-derived carbon layers, thus impeding potassium-ion diffusion. Beyond 1.0 V, the D_{K^+} value increased sharply, attributed to the conversion of nickel sulfide into ultrafine metallic Ni and potassium sulfides, as supported by CV curve in Fig. 6A. Subsequently, a slight decrease in D_{K^+} values around 0.4 V was observed, corresponding to the formation of SEI layers. During the initial depotassiation process, D_{K^+} values rose noticeably at approximately 1.2 and 1.8 V. As verified by CV curve in Fig. 6A, these increases corresponded to the stepwise reversibility of K_xNiS_y and NiS_x, respectively, which could facilitate improved potassium-ion diffusivity.

The electrochemical properties of NiS@C-CA/EG/DMF-800, NiS-CA/EG/DMF-800, NiS-CA-800, and NiS-Suc-800 were compared to highlight the advantages of uniform size distribution, yolk–shell architecture, and carbon coating, as illustrated in Fig. 7. The cycling performances of these electrodes were evaluated at a current density of 0.2 A g^{-1} (Fig. 7A). NiS-CA-800 electrode exhibited a sharp capacity drop after 30 cycles, indicating structural instability attributed to its hollow microsphere morphology with a thin shell. In contrast, NiS-Suc-800 electrode initially exhibited lower capacity than NiS-CA/EG/DMF-800 but gradually increased until 70 cycles. This behavior was likely due to the progressive disintegration of non-uniform yolk–shell microspheres, especially those with thin and wide shells, which facilitated the formation of additional SEI layers. However, beyond 70 cycles, NiS-

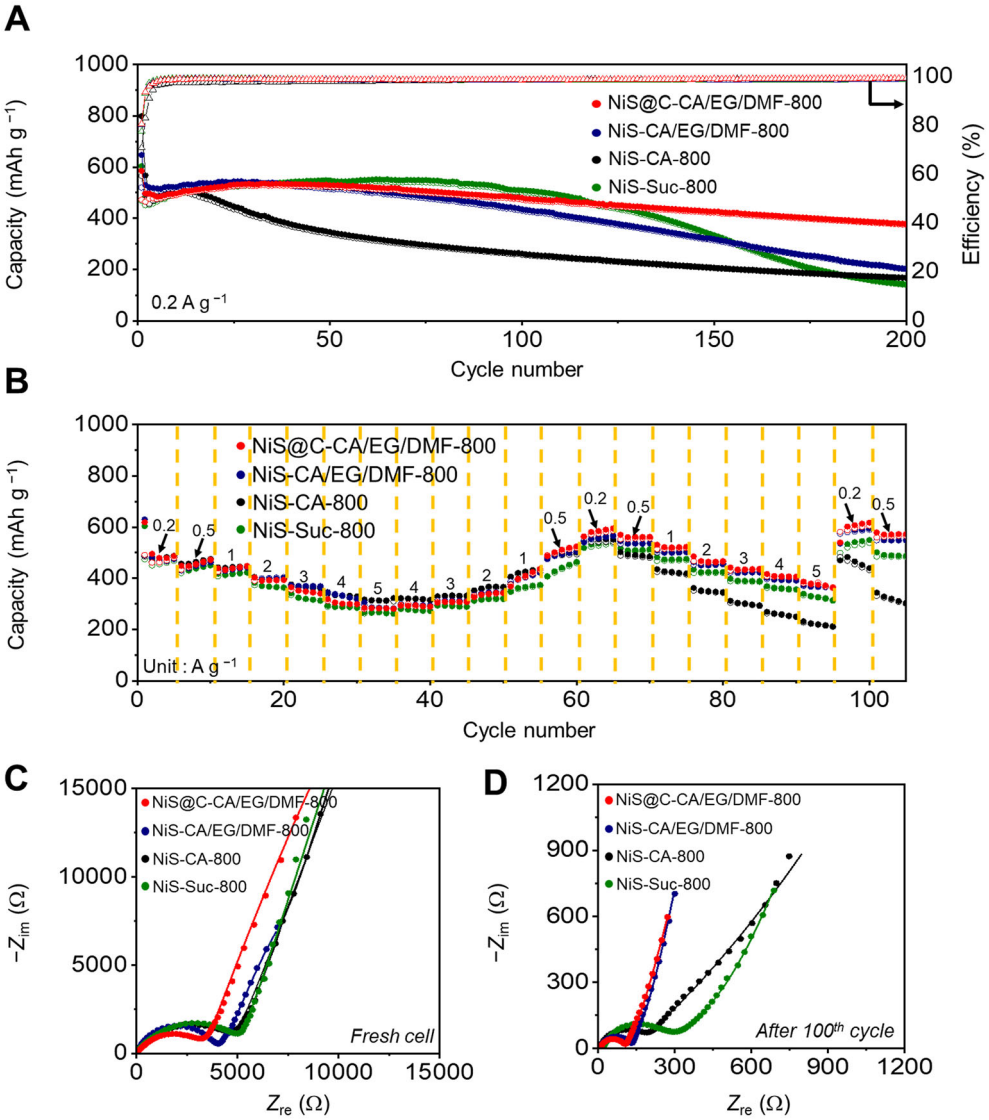

Fig. 7 Electrochemical performances of NiS@C-CA/EG/DMF-800, NiS-CA/EG/DMF-800, NiS-CA-800, and NiS-Suc-800: **A** cycling performance at a current density of 0.2 A g^{-1} and **B** rate performance. Nyquist plots (measured points and fitted lines) of **C** fresh cells and **D** cells after 100 cycles

Suc-800 exhibited a steady decline in capacity up to 200 cycles due to structural degradation. Meanwhile, NiS-CA/EG/DMF-800 exhibited a relatively modest capacity increase compared to NiS-Suc-800 but maintained a stable capacity decline after 50 cycles. Despite rapid volume changes during the potassiation and depotassiation processes, the uniform yolk–shell structure of NiS-CA/EG/DMF-800 provided superior cycling stability relative to the non-uniform yolk–shell counterpart. To further improve cyclic stability and electrical conductivity, a pitch-derived carbon coating was applied to NiS-CA/EG/DMF-800, yielding NiS@C-CA/EG/DMF-800 electrode. The stability of its cycling performance significantly improved, as shown in Fig. 7A. After 200 cycles, the discharge capacities of NiS-CA-800, NiS-Suc-800, NiS-CA/EG/DMF-800, and NiS@C-CA/EG/DMF-800 were 167.21, 142.27, 202.4, and 377.38 mAh g^{-1}, respectively, with corresponding capacity retentions from the second cycle of 83%, 93%, 94%, and 94%, respectively.

The rate performances of the four electrodes are presented in Fig. 7B. The current density was varied from 0.2 to 5 A g^{-1} in triplicate tests. During the initial rate increase, NiS-CA-800 electrode exhibited excellent rate capability, likely due to its thin-shelled hollow structure, which promotes rapid potassium-ion transport [75]. However, during subsequent rate variation tests, its performance

deteriorated rapidly due to structural collapse. In contrast, NiS@C-CA/EG/DMF-800, with its uniform yolk–shell structure and improved electrical conductivity, consistently delivered the best rate performance throughout the tests. Specifically, NiS@C-CA/EG/DMF-800 achieved reversible discharge capacities of 487.0, 473.0, 447.8, 394.0, 340.5, 298.9, and 281.1 mAh g^{-1} at current densities of 0.2, 0.5, 1, 2, 3, 4, and 5 A g^{-1}, respectively.

To verify the electrochemical stability of NiS@C-CA/EG/DMF-800, ex situ TEM and SEM analyses were conducted after 100 cycles. As depicted in Fig. S15A, B, the overall microsphere morphology was largely preserved, though the internal structure had transformed into ultrafine nanocrystals due to conversion reactions. These morphological changes, resulting from repeated volume fluctuations, demonstrate the yolk–shell structure's capacity to absorb mechanical stress without collapse. Furthermore, TEM images in Fig. S15C revealed a distinct carbon coating layer on the outer shell, further underscoring its role in enhancing structural stability and electrochemical performance. In contrast, SEM images of NiS-CA/EG/DMF-800, NiS-CA-800, and NiS-Suc-800 after 100 cycles showed substantial structural degradation and particle fracture, indicating their limited capacity to withstand repeated conversion reactions. The observed structural degradation in the comparative samples highlights the critical role of uniform architecture and carbon coating in maintaining electrode integrity. These design advantages collectively contributed to the superior electrochemical performance of NiS@C-CA/EG/DMF-800.

To further validate the electrochemical superiority of NiS@C-CA/EG/DMF-800 electrode, ex situ electrochemical impedance spectroscopy (EIS) tests were conducted on all four electrodes before and after 100 cycles, as shown in Fig. 7C, D. The data were fitted using an equivalent circuit model presented in Fig. S17. This equivalent circuit comprises R_s, R_{SEI}, R_{ct1}, and R_{ct2}, corresponding to the resistances of the electrolyte, solid–electrolyte interphase (SEI), and charge transfer, respectively. The constant phase elements CPE_{SEI}, CPE_{ct1}, and CPE_{ct2} represent the SEI capacitance and the electrical double-layer capacitance. Z_w denotes the Warburg impedance associated with ion diffusion. The Nyquist plots exhibited compressed semicircles in the medium-frequency range, corresponding to R_{ct}, R_S, and R_{SEI}, which together contribute to the total resistance ($R_t = R_{ct} + R_s + R_{SEI}$). Among all samples, NiS@C-CA/EG/DMF-800 electrode exhibited the lowest R_t value before cycling, attributed to the improved conductivity provided by the thin pitch-derived carbon coating. Notably, the EIS data exhibit a decrease in resistance after the 100th cycle for all nickel sulfide electrodes. During the discharge process, nickel sulfide reacts with K^+ ions to form ultrafine potassium sulfide and metallic Ni, and this conversion reaction significantly reduces R_t. To further support these observations, additional EIS was measured after the first cycle, as shown in Fig. S18. Consistent with the results obtained after 100 cycles, all three samples exhibited a noticeable reduction in overall resistance after the first cycle. Compared to the fresh cells, the substantial resistance decrease observed after 100 cycles is attributed to the structural transformation of the anode materials into ultrafine nanocrystals. The D_{K^+} was calculated from the sloping region in the low-frequency domain using Eq. (2):

$$D_{K^+} = 0.5(RT/Sn^2F^2C\sigma)^2 \quad (2)$$

where R is the gas constant, T is the standard temperature, S is the effective surface area of the electrode, n is the electron transport ratio during the discharge/charge process, F is Faraday's constant, C is the molar density of Li-ion in the electrode, and σ is the diffusion constant obtained from Warburg lines in Ω $s^{-1/2}$. Before cycling, NiS@C-CA/EG/DMF-800 also demonstrated the highest D_{K^+} value, owing to its structurally stable yolk–shell morphology and conductive carbon layer. After 100 cycles, all electrodes showed increased D_{K^+} values due to nanostructure transformation, with NiS@C-CA/EG/DMF-800 retaining the highest value, further confirming its superior structural integrity and sustained ion transport efficiency. The total resistance and diffusion coefficients of all electrodes, both in the fresh state and after 100 cycles, are summarized in Table S5.

To demonstrate the superior K-ion storage performance of NiS@C-CA/EG/DMF-800, CV measurements were taken for NiS@C-CA/EG/DMF-800, NiS-CA-800, and NiS-Suc-800 at scan rates of 0.1, 0.2, 0.4, 0.6, 0.8, 1.0, 1.5, and 2.0 mV s^{-1} within the potential range of 0.001−3 V, as shown in Fig. 8. With scan rate increasing, CV curves of NiS@C-CA/EG/DMF-800 electrode exhibited only slight shifts, indicating lower polarization during rapid potassiation and depotassiation compared to NiS-CA-800 and NiS-Suc-800, as shown in Fig. 8A–C. According to the power–law relationship between the peak current (i_p) and scan rate (v), expressed as $i_p = av^b$, the b-value reveals the charge storage mechanism: b-value of 1 indicates a capacitive process, while a b-value of 0.5 suggests diffusion-controlled behavior [76]. lg–lg plots of i vs. v were used to determine b-values for the cathodic (peak I) and anodic (peaks II and III) processes for all three electrodes, as shown in Fig. 8D–F. The b-values of NiS@C-CA/EG/DMF-800, NiS-CA-800, and NiS-Suc-800 for the three peaks were calculated as 0.89/0.71/0.84 (peak I), 0.91/0.64/0.86 (peak II), and 0.96/0.80/0.87 (peak III), respectively. These values confirm that the uniform yolk–shell microsphere structure and conductive carbon layers promoted smaller crystal sizes and a more exposed active surface area. The excellent electrochemical kinetics of NiS@C-

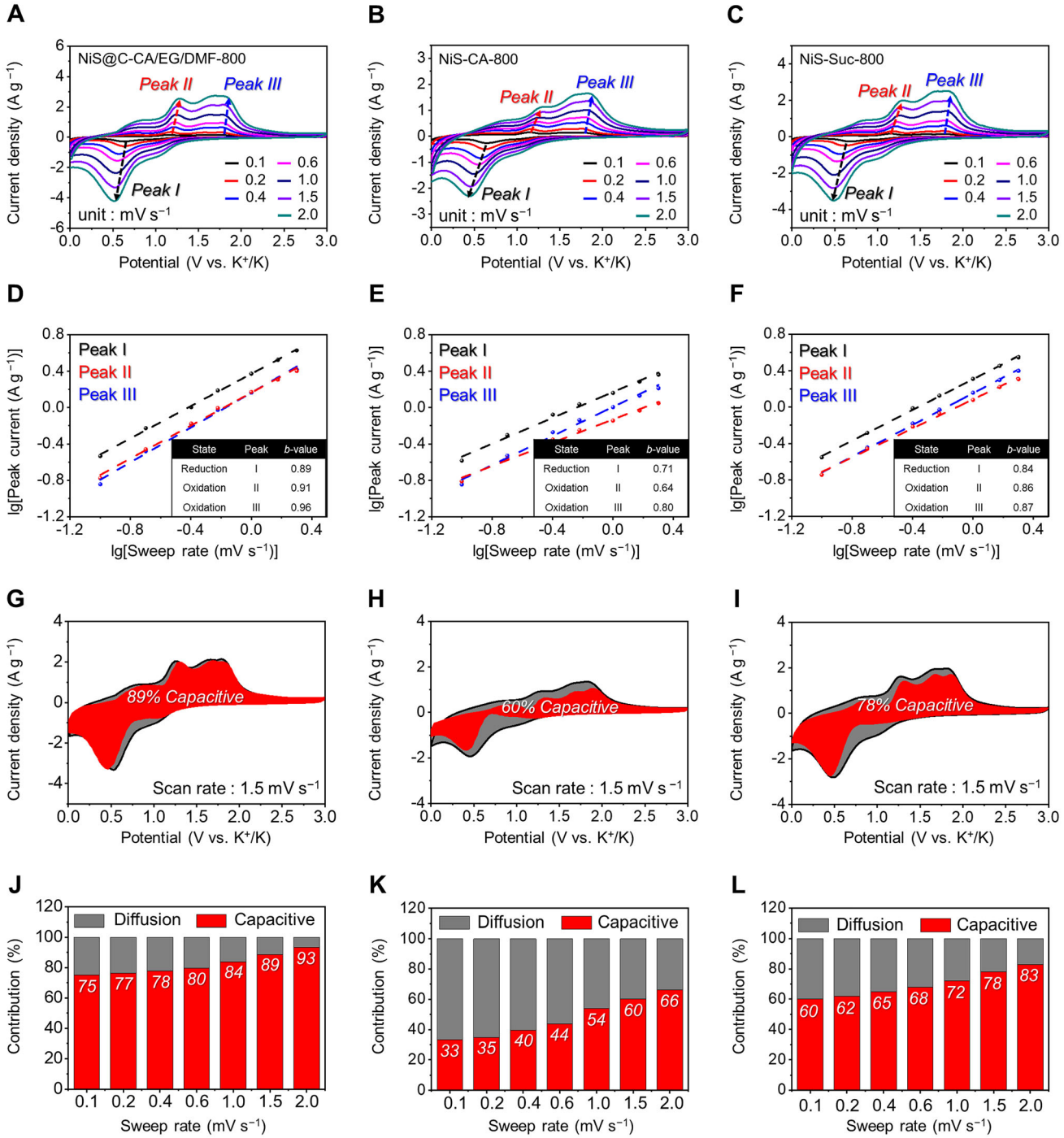

Fig. 8 Potassium-ion storage kinetic analysis: **A**–**C** CV curves at various sweep rates, **D**–**F** fitted lg (peak current) vs. lg (scan rate) of peak I, peak II, and peak III, **G**–**I** CV curves showing capacitive contribution (red-color area) to the total current at a scan rate of 1.5 mV s^{-1}, and **J**–**L** capacity contribution at different scan rate: **A**, **D**, **G**, **J** NiS@C-CA/EG/DMF-800, **B**, **E**, **H**, **K** NiS-CA-800, and **C**, **F**, **I**, **L** NiS-Suc-800

CA/EG/DMF-800, dominated by capacitive behavior, accounted for its superior rate performance, as also shown in Fig. 7B.

To further analyze the charge storage mechanism, the capacitive contribution was quantified using the equation $i(V) = k_1 v + k_2 v^{1/2}$, where $k_1 v$ and $k_2 v^{1/2}$ correspond to the surface-controlled (capacitive) process and diffusion-controlled contribution, respectively. At a scan rate of 1.5 mV s^{-1}, the capacitive contributions (shown in red) were calculated to be 89%, 60%, and 78% for NiS@C-CA/EG/DMF-800, NiS-CA-800, and NiS-Suc-800, respectively, as illustrated in Fig. 8G–I. This contribution

increased with the scan rate, reaching 93% at 2.0 mV s^{-1}, further validating the outstanding rate capability of NiS@C-CA/EG/DMF-800, as shown in Fig. 8J–L. As summarized in Table S6, the electrochemical performance of NiS@C-CA/EG/DMF-800 surpasses that of previously reported anode materials based on similar compositions for potassium-ion batteries.

4 Conclusion

Yolk–shell structures have attracted considerable interest due to their distinctive core@void@shell architecture and broad applicability in various scientific and engineering fields. This study presents a novel and scalable one-pot spray pyrolysis method, enhanced through in situ polymerization, and the use of drying control chemical agents. By systematically evaluating different carbon sources, the study elucidates their critical role in governing the size distribution and structural uniformity of yolk–shell particles. Moreover, the proposed formation mechanism, based on the intermediate formation of metal–metal oxide–carbon composites, offers valuable insights for designing yolk–shell structures with enhanced properties. The successful synthesis of nickel oxide yolk–shell particles, subsequently converted into nickel sulfide@C microspheres, underscores the potential of this strategy for energy storage, particularly as high-performance anode materials in potassium-ion batteries. This approach addresses key limitations of traditional techniques and provides a rapid, efficient route for producing yolk–shell structures with precise control over morphology and size. The insights and methodology outlined in this work open new avenues for the scalable fabrication of yolk–shell materials tailored to diverse advanced applications.

Acknowledgements This work was financially supported by the National Research Foundation of Korea (NRF) from the Korea government (MSIT) (No. RS-2023-00217581) and the Commercialization Promotion Agency for R&D Outcomes (COMPA) from the Korean Government (the Ministry of Science and ICT) (No. RS-2023-00304768).

Author contributions Tae Ha Kim designed the study and helped in methodology; formal analysis; writing original draft. Sang-Hyun Kim curated the data; performed experiments; collected data. Jung Sang Cho and Yun Chan Kang helped in writing; review and editing. Gi Dae Park helped in supervision; writing; review and editing.

Data availability The data that support the findings of this study are available from the corresponding author upon reasonable request.

Declarations

Conflict of interests The authors declare that they have no conflict of interest.

References

[1] Lin LS, Song J, Yang HH, Chen X. Yolk–shell nanostructures: design, synthesis, and biomedical applications. Adv Mater. 2018;30(6):1704639. https://doi.org/10.1002/adma.201704639.

[2] Priebe M, Fromm KM. Nanorattles or yolk–shell nanoparticles—what are they, how are they made, and what are they good for? Chem-Eur J. 2015;21(10):3854–74. https://doi.org/10.1002/chem.201405285.

[3] Liu J, Qiao SZ, Chen JS, Lou XWD, Xing X, Lu GQM. Yolk/shell nanoparticles: new platforms for nanoreactors, drug delivery and lithium-ion batteries. Chem Commun. 2011;47(47):12578–91. https://doi.org/10.1039/C1CC13658E.

[4] Guo Y, Feng L, Wu C, Wang X, Zhang X. Synthesis of 3D-ordered macro/microporous yolk–shelled nanoreactor with spatially separated functionalities for cascade reaction. ACS Appl Mater Interfaces. 2019;11(37):33978–86. https://doi.org/10.1021/acsami.9b11578.

[5] Chen H, Shen K, Mao Q, Chen J, Li Y. Nanoreactor of MOF-derived yolk–shell Co@C–N: precisely controllable structure and enhanced catalytic activity. ACS Catal. 2018;8(2):1417–26. https://doi.org/10.1021/acscatal.7b03270.

[6] Liu J, Qiao SZ, Budi Hartono S, Lu GQ. Monodisperse yolk–-shell nanoparticles with a hierarchical porous structure for delivery vehicles and nanoreactors. Angew Chem Int Ed Engl. 2010;49(29):4981–5. https://doi.org/10.1002/anie.201001252.

[7] Ji Y, Song S, Li X, Lv R, Wu L, Wang H, Cao M. Facile fabrication of nanocarriers with yolk-shell mesoporous silica nanoparticles for effective drug delivery. J Drug Deliv Sci Technol. 2021;63:102531. https://doi.org/10.1016/j.jddst.2021.102531.

[8] Li S, Zheng J, Chen D, Wu Y, Zhang W, Zheng F, Cao J, Ma H, Liu Y. Yolk–shell hybrid nanoparticles with magnetic and pH-sensitive properties for controlled anticancer drug delivery. Nanoscale. 2013;5(23):11718–24. https://doi.org/10.1039/C3NR04032A.

[9] Zhao L, Liu H, Wang F, Zeng L. Design of yolk–shell Fe_3O_4@PMAA composite microspheres for adsorption of metal ions and pH-controlled drug delivery. J Mater Chem A. 2014;2(19):7065–74. https://doi.org/10.1039/C4TA00976B.

[10] Song J, Yan P, Luo L, Qi X, Rong X, Zheng J, Xiao B, Feng S, Wang C, Hu Y-S. Yolk-shell structured Sb@C anodes for high energy Na-ion batteries. Nano Energy. 2017;40:504–11. https://doi.org/10.1016/j.nanoen.2017.08.051.

[11] Seh ZW, Li W, Cha JJ, Zheng G, Yang Y, McDowell MT, Hsu P-C, Cui Y. Sulphur-TiO_2 yolk-shell nanoarchitecture with internal void space for long-cycle lithium-sulphur batteries. Nat Commun. 2013;4:1331. https://doi.org/10.1038/ncomms2327.

[12] Zhang H, Huang X, Noonan O, Zhou L, Yu C. Tailored yolk–shell Sn@C nanoboxes for high-performance lithium storage. Adv Funct Mater. 2017;27(8):1606023. https://doi.org/10.1002/adfm.201606023.

[13] Ma X, Tang K-L, Yang M, Shi W, Zhao W. Metal–organic framework-derived yolk–shell hollow Ni/NiO@C microspheres for bifunctional non-enzymatic glucose and hydrogen peroxide biosensors. J Mater Sci. 2021;56:442–56. https://doi.org/10.1007/s10853-020-05236-8.

[14] Patel SK, Anwar MZ, Kumar A, Otari SV, Pagolu RT, Kim S-Y, Kim I-W, Lee J-K. Fe_2O_3 yolk-shell particle-based laccase biosensor for efficient detection of 2, 6-dimethoxyphenol. Biochem Eng J. 2018;132:1–8. https://doi.org/10.1016/j.bej.2017.12.013.

[15] Cheng X, Zhao H, Huang W, Chen J, Wang S, Dong J, Deng Y. Rational design of yolk–shell CuO/silicalite-1@mSiO_2 composites for a high-performance nonenzymatic glucose biosensor.

Langmuir. 2018;34(26):7663–72. https://doi.org/10.1021/acs.langmuir.8b01051.
[16] Li Y, Du R, Li W, Li J, Yang H, Bai H, Zou M, Xi G. δ-MoN yolk microspheres with ultrathin nanosheets for a wide-spectrum, sensitive, and durable surface-enhanced Raman scattering substrate. Anal Chem. 2021;93(36):12360–6. https://doi.org/10.1021/acs.analchem.1c02181.
[17] Zhang G, Dong L, Zhang S, Liu B, Yang J. One-pot synthesis of Au@mSiO$_2$ yolk–shell nanoparticles with enhanced catalytic and surface-enhanced Raman scattering (SERS) properties. J Alloys Compd. 2021;871:159631. https://doi.org/10.1016/j.jallcom.2021.159631.
[18] Kang T, Jeong S, Kang H, Kim J, Kim H-M, Kyeong S, Lee SH, Jeong DH, Jun B-H, Lee Y-S. Fabrication of Ag nanoaggregates/SiO$_2$ yolk–shell nanoprobes for surface-enhanced Raman scattering. J Ind Eng Chem. 2015;32:34–8. https://doi.org/10.1016/j.jiec.2015.09.016.
[19] Yang Y, Liu J, Li X, Liu X, Yang Q. Organosilane-assisted transformation from core–shell to yolk–shell nanocomposites. Chem Mater. 2011;23(16):3676–84. https://doi.org/10.1021/cm201182d.
[20] Wang X, Wang Y, Yang L, Wang K, Lou X, Cai B. Template-free synthesis of homogeneous yolk–shell TiO$_2$ hierarchical microspheres for high performance lithium ion batteries. J Power Sources. 2014;262:72–8. https://doi.org/10.1016/j.jpowsour.2014.03.081.
[21] Kim JH, Kang YC, Choi YJ, Kim YS, Lee JH. Electrochemical properties of yolk–shell structured layered-layered composite cathode powders prepared by spray pyrolysis. Electrochim Acta. 2014;144:288–94. https://doi.org/10.1016/j.electacta.2014.08.015.
[22] Luo L, Lo W-S, Si X, Li H, Wu Y, An Y, Zhu Q, Chou LY, Li T, Tsung C-K. Directional engraving within single crystalline metal–organic framework particles via oxidative linker cleaving. J Am Chem Soc. 2019;141(51):20365–70. https://doi.org/10.1021/jacs.9b10499.
[23] Mi H, Yang X, Li Y, Zhang P, Sun L. A self-sacrifice template strategy to fabricate yolk–shell structured silicon@void@carbon composites for high-performance lithium-ion batteries. Chem Eng J. 2018;351:103–9. https://doi.org/10.1016/j.cej.2018.06.065.
[24] Xie Q, Li J, Tian Q, Shi R. Template-free synthesis of zinc citrate yolk–shell microspheres and their transformation to ZnO yolk–shell nanospheres. J Mater Chem. 2012;22(27):13541–7. https://doi.org/10.1039/C2JM31243C.
[25] Ma W, He P, Xu J, Liu X, Lin S, Cui ZK, Zuo P, Zhuang Q. Self-assembly magnetized 3D hierarchical graphite carbon-based heterogeneous yolk–shell nanoboxes with enhanced microwave absorption. J Mater Chem A. 2022;10(21):11405–13. https://doi.org/10.1039/D2TA01798A.
[26] Zhang L, Wang H. Interior structural tailoring of Cu$_2$O shell-in-shell nanostructures through multistep Ostwald ripening. J Phys Chem C. 2011;115(38):18479–85. https://doi.org/10.1021/jp2059613.
[27] Liu J, Yu L, Wu C, Wen Y, Yin K, Chiang FK, Hu R, Liu J, Sun L, Gu L. New nanoconfined galvanic replacement synthesis of hollow Sb@C yolk–shell spheres constituting a stable anode for high-rate Li/Na-ion batteries. Nano Lett. 2017;17(3):2034–42. https://doi.org/10.1021/acs.nanolett.7b00083.
[28] Cho JS, Kang YC. Nanofibers comprising yolk–shell Sn@void@SnO/SnO$_2$ and hollow SnO/SnO$_2$ and SnO$_2$ nanospheres via the Kirkendall diffusion effect and their electrochemical properties. Small. 2015;11(36):4673–81. https://doi.org/10.1002/smll.201500940.
[29] Liang X, Li J, Joo JB, Gutiérrez A, Tillekaratne A, Lee I, Yin Y, Zaera F. Diffusion through the shells of yolk–shell and core–shell nanostructures in the liquid phase. Angew Chem Int Ed. 2012;51(32):8034–6. https://doi.org/10.1002/anie.201203456.
[30] Wang G-H, Chen K, Engelhardt J, Tüysüz H, Bongard H-J, Schmidt W, Schüth F. Scalable one-pot synthesis of yolk–shell carbon nanospheres with yolk-supported Pd nanoparticles for size-selective catalysis. Chem Mater. 2018;30(8):2483–7. https://doi.org/10.1021/acs.chemmater.8b00456.
[31] Hong YJ, Son MY, Kang YC. Batteries: one-pot facile synthesis of double-shelled SnO$_2$ yolk-shell-structured powders by continuous process as anode materials for li-ion batteries. Adv Mater. 2013;25(16):2279–83. https://doi.org/10.1002/adma.201204506.
[32] Liang H, Wang Z, Guo H, Li X. Unique porous yolk-shell structured Co$_3$O$_4$ anode for high performance lithium ion batteries. Ceram Int. 2017;43(14):11058–64. https://doi.org/10.1016/j.ceramint.2017.05.150.
[33] Zhang Y, Su Y, Wang Y, He J, McPherson GL, John VT. Rapid fabrication of hollow and yolk–shell α-Fe$_2$O$_3$ particles with applications to enhanced photo-Fenton reactions. RSC Adv. 2017;7(62):39049–56. https://doi.org/10.1039/C7RA06621J.
[34] Kim YB, Kim TH, Kim S, Jeong S, Kang YC, Lee D, Park GD. Multiple heteroatom-doped cobalt sulfoselenide@C yolk-shell microsphere as excellent anode materials for sodium-ion batteries and their conversion reaction mechanism with sodium ions. J Power Sources. 2024;618:235186. https://doi.org/10.1016/j.jpowsour.2024.235186.
[35] Kim JH, Kang YC. Synthesis of uniquely structured yolk-shell metal oxide microspheres filled with nitrogen-doped graphitic carbon with excellent Li–ion storage performance. Small. 2017;13(39):1701585. https://doi.org/10.1002/smll.201701585.
[36] Peng QQ, Wang YT, Qi S, Xiao Y, Wang Y, Chen SQ. The homogenous growth of Co-based coordination compound on graphene nanosheet for high-performance K-organic battery and its reaction mechanism. Rare Met. 2024;43(4):1622–34. https://doi.org/10.1007/s12598-023-02525-4.
[37] Mu ZJ, Gao YJ, Dong WS, Li ZY, Song QY, Huang HJ, Xing LD, Zhang JG, Wang W, Yu QY. AN–CoSe/CoSe$_2$–C@Cu hierarchical architecture as a current collector-integrated anode for potassium-ion batteries. Rare Met. 2024;43(8):3702–12. https://doi.org/10.1007/s12598-024-02788-5.
[38] Zhao R, Di H, Hui X, Zhao D, Wang R, Wang C, Yin L. Self-assembled Ti$_3$C$_2$ MXene and N-rich porous carbon hybrids as superior anodes for high-performance potassium-ion batteries. Energy Environ Sci. 2020;13(1):246–57. https://doi.org/10.1039/C9EE03250A.
[39] Zhao R, Di H, Wang C, Hui X, Zhao D, Wang R, Zhang L, Yin L. Encapsulating ultrafine Sb nanoparticles in Na$^+$ pre-intercalated 3D porous Ti$_3$C$_2$T$_x$ MXene nanostructures for enhanced potassium storage performance. ACS Nano. 2020;14(10):13938–51. https://doi.org/10.1021/acsnano.0c06360.
[40] Dong X, Zhao R, Di H, Wang B, Zhao G, Gao T, Li H, Sun B, Chao D, Zhou G. Phosphorus-regulated nitrogen sites in ultrathin carbon scrolls for stable potassium storage. ACS Appl Energy Mater. 2022;5(7):8526–37. https://doi.org/10.1021/acsaem.2c01073.
[41] Romanova I, Kirillov S. Preparation of Cu, Ni and Co oxides by a citric acid-aided route: effect of metal ions on thermal decomposition and morphology. J Therm Anal Calorim. 2018;132:503–12. https://doi.org/10.1007/s10973-017-6880-5.
[42] Park GD, Lee JH, Lee JK, Kang YC. Effect of esterification reaction of citric acid and ethylene glycol on the formation of multi-shelled cobalt oxide powders with superior electrochemical properties. Nano Res. 2014;7:1738–48. https://doi.org/10.1007/s12274-014-0533-9.
[43] Jung KY, Kang YC, Park YK. DMF effect on the morphology and the luminescence properties of Y$_2$O$_3$: Eu^{3+} red phosphor

prepared by spray pyrolysis. J Ind Eng Chem. 2008;14(2):224–9. https://doi.org/10.1016/j.jiec.2007.09.011.
[44] Thaines EH, Ferreira CS, Oliveira AC, Garcia MD, Freitas RG, Passos RR, Silva EC, Pocrifka LA. Structural and electrochemical analysis of Ni/NiO supercapacitor materials: a theoretical and experimental study. Solid State Ion. 2023;394:116194. https://doi.org/10.1016/j.ssi.2023.116194.
[45] Xi Y, Huang S, Yang D, Qiu X, Su H, Yi C, Li Q. Hierarchical porous carbon derived from the gas-exfoliation activation of lignin for high-energy lithium-ion batteries. Green Chem. 2020;22(13):4321–30. https://doi.org/10.1039/D0GC00945H.
[46] Feng PX, Chen QL, Yang DJ, Wang H. Nitrogen-doped lignin mesoporous carbon/nickel/oxide nanocomposites with excellent lithium storage properties. Rare Met. 2025. https://doi.org/10.1007/s12598-024-03192-9.
[47] Tian Y, Yang Z, Wang H, Xiong W, Lin X, Wang S, Kong F, Li P, Xi Y, Zhang F. Nitrogen-doped 3D carbon hybrids based on modified lignin as sulfur host for high-performance lithium-sulfur batteries. J Power Sources. 2024;621:235322. https://doi.org/10.1016/j.jpowsour.2024.235322.
[48] Majedi A, Abbasi A, Davar F. Green synthesis of zirconia nanoparticles using the modified Pechini method and characterization of its optical and electrical properties. J Sol-Gel Sci Technol. 2016;77:542–52. https://doi.org/10.1007/s10971-015-3881-3.
[49] Ghorbani S, Razavi RS, Loghman-Estarki M, Alhaji A. Development of MgO–Y_2O_3 composite nanopowder by Pechini sol–gel method: effect of synthesis parameters on morphology, particle size, and phase distribution. J Clust Sci. 2017;28:1523–39. https://doi.org/10.1007/s10876-017-1162-8.
[50] Xiong LYZ, Liu BW, Du L, Zhou YK, Lin XL, Wang H. Bimetallic NiCoP catalysts anchored on phosphorus-doped lignin-based carbon for robust oxygen evolution performance. Rare Met. 2024;43(7):3084–95. https://doi.org/10.1007/s12598-024-02718-5.
[51] Pastoriza-Santos I, Liz-Marzán LM. Formation of PVP-protected metal nanoparticles in DMF. Langmuir. 2002;18(7):2888–94. https://doi.org/10.1021/la015578g.
[52] Gao Y, Jiang P, Song L, Wang J, Liu L, Liu D, Xiang Y, Zhang Z, Zhao X, Dou X. Studies on silver nanodecahedrons synthesized by PVP-assisted N, N-dimethylformamide (DMF) reduction. J Cryst Growth. 2006;289(1):376–80. https://doi.org/10.1016/j.jcrysgro.2005.11.123.
[53] Seo HY, Choi JH, Kim YB, Cho JS, Kang YC, Park GD. Tailoring the shell thickness of yolk–shell structured carbon microspheres: applications in metal selenide and carbon composite microspheres for enhanced sodium ion storage properties. J Mater Chem A. 2023;11(45):24738–53. https://doi.org/10.1039/D3TA04705A.
[54] Li JY, Li G, Zhang J, Yin YX, Yue FS, Xu Q, Guo YG. Rational design of robust Si/C microspheres for high-tap-density anode materials. ACS Appl Mater Interfaces. 2019;11(4):4057–64. https://doi.org/10.1021/acsami.8b20213.
[55] Pan M, Zhao M-C, Zang Q, Liu J, Atrens A, Zhang F. Insight into nanotransition metal disulfides as anode for potassium-ion batteries: applications, challenges, and prospects. Energy Mater Adv. 2024;5:0120. https://doi.org/10.34133/energymatadv.0120.
[56] Guo J, Schaefer JL, Shao Y. Rechargeable multivalent-ion batteries. Energy Mater Adv. 2024;5:0112. https://doi.org/10.34133/energymatadv.0112.
[57] Wang Z, Li Y, Zhou Q, Li Q, Zhao R, Qiu Z, Zhang R, Sun Y, Wu F, Wu C. Multi-ion strategies toward advanced rechargeable batteries: materials, properties, and prospects. Energy Mater Adv. 2024;5:0109. https://doi.org/10.34133/energymatadv.0112.
[58] Zhou J, Liu Y, Zhang S, Zhou T, Guo Z. Metal chalcogenides for potassium storage. InfoMat. 2020;2(3):437–65. https://doi.org/10.1002/inf2.12101.
[59] Wu Y, Zhang C, Zhao H, Lei Y. Recent advances in ferromagnetic metal sulfides and selenides as anodes for sodium-and potassium-ion batteries. J Mater Chem A. 2021;9(15):9506–34. https://doi.org/10.1039/D1TA00831E.
[60] Tan H, Feng Y, Rui X, Yu Y, Huang S. Metal chalcogenides: paving the way for high-performance sodium/potassium-ion batteries. Small Methods. 2020;4(1):1900563. https://doi.org/10.1002/smtd.201900563.
[61] Chen HJ, Wang Y, Ma XD, Fan C, Shen PK, Ta SW, Wu H-B, Feng ZS. Cation-adsorption-assisted Ni_3S_2/carbon nanowalls composites with three-dimensional interconnected porous structures for high-performance lithium-ion battery anodes. J Mater Sci. 2020;55:17081–93. https://doi.org/10.1007/s10853-020-05203-3.
[62] Karthikeyan R, Thangaraju D, Prakash N, Hayakawa Y. Single-step synthesis and catalytic activity of structure-controlled nickel sulfide nanoparticles. CrystEngComm. 2015;17(29):5431–9. https://doi.org/10.1039/C5CE00742A.
[63] Li L, Meng T, Wang J, Mao B, Huang J, Cao M. Oxygen vacancies boosting lithium-ion diffusion kinetics of lithium germanate for high-performance lithium storage. ACS Appl Mater Interfaces. 2021;13(21):24804–13. https://doi.org/10.1021/acsami.1c04200.
[64] Yuan J, Wen J, Zhong Y, Li X, Fang Y, Zhang S, Liu W. Enhanced photocatalytic H_2 evolution over noble-metal-free NiS cocatalyst modified CdS nanorods/g-C_3N_4 heterojunctions. J Mater Chem A. 2015;3(35):18244–55. https://doi.org/10.1039/C5TA04573H.
[65] Wang Q, Zhao X, Ni C, Tian H, Li J, Zhang Z, Mao SX, Wang J, Xu Y. Reaction and capacity-fading mechanisms of tin nanoparticles in potassium-ion batteries. J Phys Chem C. 2017;121(23):12652–7. https://doi.org/10.1021/acs.jpcc.7b03837.
[66] Liu L, Chen Y, Xie Y, Tao P, Li Q, Yan C. Understanding of the ultrastable K-ion storage of carbonaceous anode. Adv Funct Mater. 2018;28(29):1801989. https://doi.org/10.1002/adfm.201801989.
[67] Park J-S, Kang YC. Multicomponent (Mo, Ni) metal sulfide and selenide microspheres with empty nanovoids as anode materials for Na-ion batteries. J Mater Chem A. 2017;5(18):8616–23. https://doi.org/10.1039/C7TA01088E.
[68] Qin W, Chen T, Lu T, Chua DH, Pan L. Layered nickel sulfide-reduced graphene oxide composites synthesized via microwave-assisted method as high performance anode materials of sodium-ion batteries. J Power Sources. 2016;302:202–9. https://doi.org/10.1016/j.jpowsour.2015.10.064.
[69] Zhang S, Ling F, Wang L, Xu R, Ma M, Cheng X, Bai R, Shao Y, Huang H, Li D. An open-ended Ni_3S_2–Co_9S_8 heterostructures nanocage anode with enhanced reaction kinetics for superior potassium-ion batteries. Adv Mater. 2022;34(18):2201420. https://doi.org/10.1002/adma.202201420.
[70] Park GD, Cho JS, Kang YC. Sodium-ion storage properties of nickel sulfide hollow nanospheres/reduced graphene oxide composite powders prepared by a spray drying process and the nanoscale Kirkendall effect. Nanoscale. 2015;7(40):16781–8. https://doi.org/10.1039/C5NR04252F.
[71] Wu CM, Pan PI, Cheng YW, Liu CP, Chang CC, Avdeev M, Lin SK. The mechanism of the sodiation and desodiation in Super P carbon electrode for sodium-ion battery. J Power Sources. 2017;340:14–21. https://doi.org/10.1016/j.jpowsour.2016.11.048.
[72] Zhu D, Li S, Huang J, Chen Z, Hu Z, Li J, Li X, Yang H, Feng Z. Hydrothermal synthesis of Ni_3S_2/Ni@N-doped carbon for high-performance alkali metal batteries. J Alloys Compd. 2021;859:158246. https://doi.org/10.1016/j.jallcom.2020.158246.
[73] Yang L, Hong W, Zhang Y, Tian Y, Gao X, Zhu Y, Zou G, Hou H, Ji X. Hierarchical NiS_2 modified with bifunctional carbon for enhanced potassium-ion storage. Adv Funct Mater. 2019;29(50):1903454. https://doi.org/10.1002/adfm.201903454.

[74] Yao Q, Zhang J, Li J, Huang W, Hou K, Zhao Y, Guan L. Yolk–shell NiS_x@C nanosheets as K-ion battery anodes with high rate capability and ultralong cycle life. J Mater Chem A. 2019;7(32):18932–9. https://doi.org/10.1039/C9TA06292K.

[75] Li L, Zhang W, Wang X, Zhang S, Liu Y, Li M, Zhu G, Zheng Y, Zhang Q, Zhou T. Hollow-carbon-templated few-layered V_5S_8 nanosheets enabling ultrafast potassium storage and long-term cycling. ACS Nano. 2019;13(7):7939–48. https://doi.org/10.1021/acsnano.9b02384.

[76] Zhang W, Yin J, Sun M, Wang W, Chen C, Altunkaya M, Emwas AH, Han Y, Schwingenschlögl U, Alshareef HN. Direct pyrolysis of supermolecules: an ultrahigh edge-nitrogen doping strategy of carbon anodes for potassium-ion batteries. Adv Mater. 2020;32(25):2000732. https://doi.org/10.1002/adma.202000732.